Dual-plane turbulent jets and their non-Gaussian velocity fluctuations

Yi Zhou,[1,*] Koji Nagata,[2] Yasuhiko Sakai,[3] and Tomoaki Watanabe[2]
[1]*School of Energy and Power Engineering, Nanjing University of Science and Technology, Nanjing 210094, China*
[2]*Department of Aerospace Engineering, Nagoya University, Nagoya 464-8603, Japan*
[3]*Department of Mechanical Science and Engineering, Nagoya University, Nagoya 464-8603, Japan*

(Received 3 June 2018; published 10 December 2018)

Direct numerical simulations are performed to investigate the spatial evolution of dual-plane jet flows with different separation lengths between the two jets. Based on the scaling law and the probability density function of the turbulent/nonturbulent interface of a single plane jet, the jet-interaction length scale X_* is introduced. It is shown that for different separation lengths, the streamwise evolutions of various statistics along the centerline all scale with X_*. This finding may explain the linear relationship between the location of the merge point and the separation length. Of particular interest is the evolution of the probability distributions and energy spectra of the streamwise velocity fluctuations in the developing region. Similar to the case of grid-generated turbulence, the probability distribution of the velocity fluctuations can also be non-Gaussian in a dual-plane jet flow. For all flow configurations considered, close to the inlet (e.g., $X/X_* \simeq 1.0$) where the two jets have not yet joined together, the skewness of the streamwise velocity fluctuations is negative. In contrast, at a further downstream location (e.g., $X/X_* \simeq 2.0$), where the turbulence intensity and mean pressure reach their maximum values, the skewness takes a positive value instead. Our study suggests that there are two different physical mechanisms responsible for the formation of the intense oscillations of the velocity fluctuations. The negative value of the skewness in the upstream region is caused by the large-scale movement of the contrarotary vortices, whereas the streamwise position of the positive skewness appears to be correlated to the location of peak intensity near (or after) the merging of the jets.

DOI: 10.1103/PhysRevFluids.3.124604

I. INTRODUCTION

Parallel jet flows, which are also referred to as "twin jets" or "dual jets" [1,2], are widely encountered in various engineering applications [3] (e.g., burners, boilers, gas turbine combustors, fuel injection systems, exhaust stacks, etc.). The pioneer work of Miller and Comings [4] and Tanaka [5,6] revealed that three different regions (i.e., converging region, merging region, and combined region) can be identified for parallel jet flows. Bunderson *et al.* [7] investigated the possibility of passive control of the plane parallel jets by altering the jets' spacing and momentum flux ratios. By using two-dimensional unsteady Reynolds averaged Navier–Stokes (RANS) equations, Mondal *et al.* [3] numerically demonstrated that the downstream location of the merge point X_{mp} increases linearly with the separation distance between the two jets. The merge point is the streamwise location where the two inner turbulent layers merge and the corresponding mean streamwise velocity is zero. Using planar laser-induced fluorescence, Soltys and Crimaldi [8]

*Corresponding author: yizhou@njust.edu.cn

experimentally investigated the mixing and reaction between two scalars emitted from parallel jets. Baratian-Ghorghi *et al.* [9–11] experimentally studied the merging of unequal parallel turbulent jets and suggested that X_{mp} is relatively insensitive to the momentum flux ratio.

Besides jets, the other commonly studied turbulent free shear flows are wakes and mixing layers. The free shear flows (jets, wakes, and mixing layers) possess similar characteristics (i.e., self-similarity and turbulent/nonturbulent interfaces at their edges). As a matter of fact, compared with the case of jet interactions, the turbulent flows due to wake interactions (e.g., grid-generated turbulence) are more widely investigated for the reason that in the far downstream region of a grid the turbulence is thought to be quasihomogeneous and isotropic [12]. Over the past ten years, turbulent flows generated by regular and fractal grids have been extensively studied both experimentally [13–19] and numerically [20–28]. It was demonstrated that in the upstream region of grid-generated turbulence, distributions of the velocity fluctuations are highly non-Gaussian [14,16,19,21–23,26,28]. The term "highly non-Gaussian" refers to the observation that the probability density functions (PDFs) of the streamwise velocity fluctuations u' have significant fat tails compared with the Gaussian fit (see, for example, Fig. 13 in the work of Mazellier and Vassilicos [14], Fig. 13 in the paper by Zhou *et al.* [26], and Fig. 7 in the study by Laizet *et al.* [22]), which means that the probability of rare events (i.e., intense value of u') is much larger than the corresponding Gaussian distribution. In other words, the kurtosis of u' is much larger than that of a Gaussian distribution. The turbulent motions contributing to the fat PDF profiles are often referred to as extreme events [14] or intense events [22]. Moreover, the profiles of the PDFs are skewed to the left side (i.e., negatively skewed) instead of being symmetrical, suggesting that the fluctuations tend to have intense negative values [14,21–23,28]. And the corresponding vortex clusters (i.e., high-enstrophy regions) are intermittently distributed in space (refer to Figs. 22 and 23 in the paper by Zhou *et al.* [26] and Fig. 10 in the study by Laizet *et al.* [22]).

It is worth mentioning that the negatively skewed and non-Gaussian distributions of the velocity fluctuations are found to be intimately associated with the interscale energy transfer [22,23,26–28]. To the best of our knowledge, Laizet *et al.* [20] performed the first numerical study on the spatial evolution of interscale energy transfer in a fractal-generated turbulent flow. Following their pioneering work, further investigations [18,22,26] on the interscale energy transfer in grid-generated turbulence (i.e., stirred by fractal square [17,18,28] and single square [22,26] grids) are carried out. One important finding is that a $2/3$ power law of the second-order structure function (or equivalently $-5/3$ power law in the wave-number space) can be clearly observed at a location where the fluctuation distribution is significantly negatively skewed and the local Reynolds number is still considerably low [22,26,28]. Also it is found that the range of the $-5/3$ power law is gradually eroded with increasing downstream distance [20,22,26,28]. The physical mechanism responsible for the non-Gaussian distributions of u' in grid-generated turbulent flows, however, is still unclear. Also, the deterioration of the power-law range with downstream distance is not well understood yet.

In the first part of the paper, we study the influences of different separation lengths between the two jets. Previous studies revealed that in the near field of grid-generated turbulence, large-scale wakes interact with each other and non-Gaussian distributions of u' with negative skewness can be found [21,23,26,28]. Several questions naturally arise: Can non-Gaussian distributions of velocity fluctuations also be found in the turbulence generated by jet interactions? If non-Gaussian distributions exist, how are these distributions similar to and different from the case of grid-generated turbulence? What physical mechanisms are responsible for these non-Gaussian distributions? In the second part of the paper, we are trying to give answers to these questions. To shed light on the physical mechanism which excites the non-Gaussian distributions, we study dual-plane jet flows instead of simply repeating the investigation of grid-generated turbulence. Note that in the lee of a grid (either a fractal or a regular one), the turbulent flow contains both wakes and jets, which would interact with their neighbors and stir turbulence. Therefore, this study will also help to elucidate the physical characteristics of grid-generated turbulence, at least in the upstream region. This part of the work to some extent can be viewed as a continuation of our previous investigations [23,26,27].

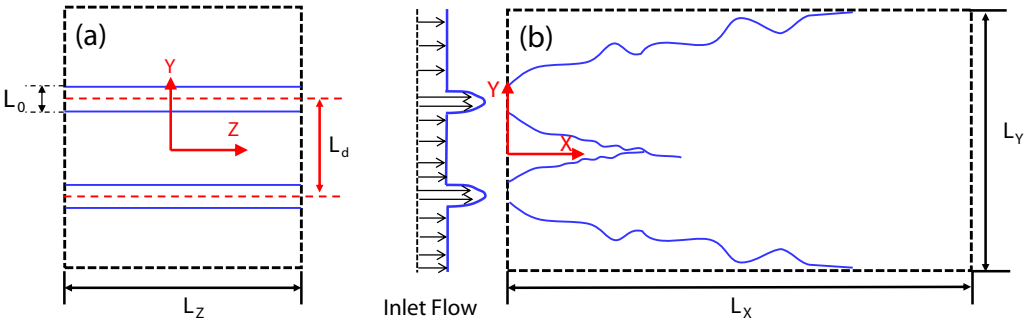

FIG. 1. (a) Schematic front view and (b) schematic side view of the computational domain. The two drawings are not to scale.

The organization of this paper is as follows. The details about the simulation conditions and numerical method are presented in Sec. II. In Sec. III, the jet-interaction length scale is introduced and discussed. In Sec. IV, the statistical results are presented and explanations for the formation of the non-Gaussian distributions of velocity fluctuations are proposed. The information on the energy spectra and small-scale intermittency is also given. Finally, the main conclusions and the remaining issues, which should be addressed in future, are listed in Sec. V.

II. NUMERICAL DETAILS

A. Computational parameters and spatial discretization

In the current direct numerical simulations (DNS) study of dual-plane jet flows, the first of its kind, we perform simulations with three different separation distances L_d between the two parallel plane jets (i.e., $L_d/L_0 = 4$, 6, and 8), where L_0 is the width of jet. A schematic view of the computational domain is presented in Fig. 1 along with the coordinate system. The coordinates X, Y, and Z refer to the streamwise, vertical, and spanwise directions, respectively. The lengths of the simulation domain in the X, Y, and Z directions, respectively, are L_X, L_Y, and L_Z. The origin of the coordinate system is located at the center of inlet plane. The exits of two plane jets are placed at $Y = (1/2)L_d$ and $-(1/2)L_d$, respectively. The simulation parameters for all three cases are given in Table I. To fully resolve the velocity field, the inlet Reynolds number Re_{L_0} based on the mean velocity at the center of the inlet slot U_J and the width of jet L_0 is set to 2000, which is comparable with previous DNS studies (e.g., $\mathrm{Re}_{L_0} = 2200$ in the work of Watanabe *et al.* [29–31] and $\mathrm{Re}_{L_0} = 3000$ in the papers by Stanley *et al.* [32] and da Silva and Métais [33]). A uniformly distributed steamwise ambient velocity $U_A/U_J = 0.1$, which is the same as that in the DNS by Stanley *et al.* [32], is imposed at the inlet (i.e., $X/L_0 = 0$) as coflow. A quite similar magnitude of coflow $U_A/U_J = 0.091$ was used by da Silva and Métais [33]. Previous numerical studies [32,33] have demonstrated that such a small amplitude of coflow exerts a very small influence on the evolution of the jet dynamics.

TABLE I. Simulation parameters.

Run	Re_{L_0}	U_A/U_J	L_d/L_0	L_X/L_0	L_Y/L_0	L_Z/L_0	N_X	N_Y	N_Z
JI4	2000	0.10	4	30	40	8	701	801	120
JI6	2000	0.10	6	30	40	8	701	801	120
JI8	2000	0.10	8	30	50	8	701	801	120

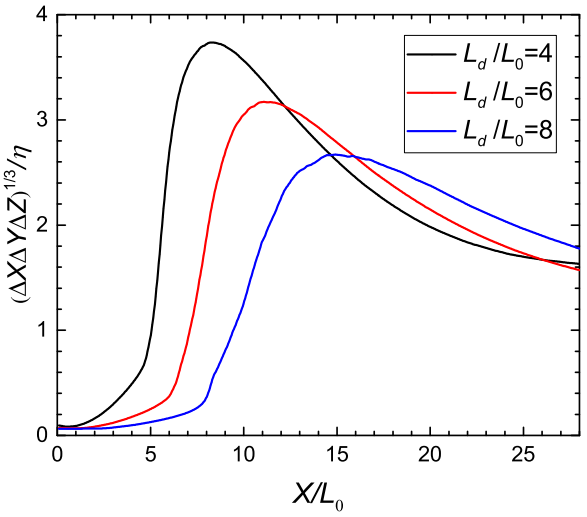

FIG. 2. Streamwise evolution of the spatial resolution $(\Delta X \Delta Y \Delta Z)^{1/3}/\eta$ along the centerline.

Uniform meshes with equal node space are used in the X and Z directions. To increase the spatial resolution in the Y direction, a nonuniform grid with concentrating points around the centerline (i.e., $Y/L_0 = 0$) is employed. The spatial resolutions with respect to the Kolmogorov microscale, which is commonly viewed as the smallest turbulent scale, $(\Delta X \Delta Y \Delta Z)^{1/3}/\eta$, along the centerline for all three cases are presented in Fig. 2. As summarized in the review paper by Moin and Mahesh [34] for incompressible turbulent flows, "the smallest resolved lengthscale is required to be of $O(\eta)$, not equal to η" (p. 544). Recently, Laizet *et al.* [21] investigated the influences of the spatial resolution in a similar flow configuration (the turbulent flow behind a single square grid) by comparing experimental and numerical results. They have confirmed that a resolution of $\Delta \simeq 7\eta$ is fine enough to guarantee high-order statistics (i.e., skewness and kurtosis of velocity fluctuations) within an error less than 10%. Note that they used the same DNSs solver INCOMPACT3D as the present study. As shown in Fig. 2, the spatial resolutions are at worse 3.7, 3.1, and 2.6, respectively, which somehow confirms that the current mesh size is fine enough to accurately capture the statistics that we are interested in for all three cases.

B. Boundary conditions

Here, we use similar boundary conditions as those in the simulation of a planer jet by Watanabe *et al.* [29–31]. They confirmed the validity of those boundary settings by comparing numerical and experimental results [29–31].

Inflow/outflow conditions are adopted in the X direction. At every time step, velocity profiles have to be imposed at the inlet of the simulation domain (i.e., $X/L_0 = 0$). The velocity fluctuations superimposed to a mean velocity profile are used as inlet velocity. To effectively trigger three-dimensional instabilities and speed up the transition from laminar to turbulent flow, various methods (e.g., inverse Fourier transform [32], digital filter [35], diffusion process [36], auxiliary simulation [37]) are proposed. In this study, an auxiliary numerical simulation of a channel flow is performed and the fully developed DNS data are used to approximate the velocity at the jet exit (i.e., $X/L_0 = 0$). The Reynolds number based on the centerline velocity and the width of the channel is set to 4000. This is because at a smaller Reynolds number $\mathrm{Re}_{L_0} = 2000$, the channel flow is laminar. In other words, the turbulence cannot maintain itself at such a low Reynolds number owing to the significant viscous dissipation and consequently the flow in the channel flow will finally evolve to a laminar state no matter how strong initial disturbances are imposed. Meanwhile, to avoid any significant

contaminations and to allow a natural transition, relatively small-amplitude fluctuations (u'_{jet}, v'_{jet}, and w'_{jet}) are superimposed to the combination of the mean velocity profiles of the auxiliary channel flow and the ambient flow as the instantaneous input jet velocity. That is only one-fifth of the strength of the auxiliary channel turbulence (i.e., $u'_{\text{jet}} = u'_c/5$, $v'_{\text{jet}} = v'_c/5$, and $w'_{\text{jet}} = w'_c/5$ with u'_c, v'_c, and w'_c being the corresponding streamwise, vertical, and spanwise velocity fluctuations of the auxiliary channel flow based on Taylor's frozen hypothesis) are imposed at the input jet to trip the turbulence. The inlet mean streamwise velocity is $U_{\text{in}} = U_J + U_A$ for the two input jets and $U_{\text{in}} = U_A$ otherwise, where $U_J(Y)$ is the vertical distribution of the mean streamwise velocity of the auxiliary simulation of the channel flow. The mean velocity in the Y and Z directions (i.e., V_{in} and W_{in}) at $X/L_0 = 0$ are set to zero. The convective outflow condition $\frac{\partial u_i}{\partial t} + U_m \frac{\partial u_i}{\partial X} = 0$ is applied at the outlet (i.e., $X/L_0 = 30$) with U_m being the characteristics advective velocity. To some extent, the choice of U_m is arbitrary since there are several different ways to decide U_m [38]. To achieve a better global mass conservation, U_m is set to be the average between the instantaneous minimum and maximum value at the outlet [39].

Owing to the existence of the entrainment process, it is important to allow momentum exchanges between the simulation domain and the outside domain across the normal boundaries [i.e., $Y = \pm(1/2)L_Y$]. The derivatives of all three velocity components with respect to the Y direction are set to zero, $\partial u/\partial Y = \partial v/\partial Y = \partial w/\partial Y = 0$, to allow a natural development of the free outside turbulent/nonturbulent interfaces.

Finally, the boundary condition in the Z direction is periodic [take, for instance, for the instantaneous streamwise velocity $u(X, Y, Z + L_z) = u(X, Y, Z)$], which is a natural choice for the simulation of two-dimensional shear flows.

C. Numerical techniques and validation

To solve Navier-Stokes equations with a constant kinematic viscosity ν and flow density ρ, we use the massively parallel solver INCOMPACT3D based on a Cartesian mesh [40–42]. Concerning the spatial discretization, sixth-order central compact schemes proposed by Lele [43] are used. A fractional step method is adopted to ensure incompressibility [44], and the resulting Poisson equation is solved in spectral space. More specifically, the two-dimensional (2D) decomposition library code (2DECOMP&FFT library) [42], which provides efficient interface to perform three-dimensional distributed FFTs, is adopted to solve the pressure Poisson equation. By using the concept of the modified wave number, the incompressibility can be ensured up to the machine accuracy ($\sim 10^{-14}$) [40]. To reduce the residual aliasing errors, a small amount of extra numerical dissipation is added at small scales (i.e., the highest wave numbers) [43,45]. Meanwhile, the differentiation of the viscous term still preserves sixth-order accuracy. The third-order Adams-Bashforth scheme is adopted for the time advancement with a time step $\Delta t = 0.006 L_0/U_J$ and data are averaged over 10^5 time steps for all three cases. Throughout this work, the statistical average is taken over time by using data at each time step and over the approximately statistically homogeneous direction Z unless otherwise indicated. The validation of statistical convergence is presented in the appendix. The maximum Courant-Friedrichs-Levy number in this simulation study is 0.17. For a complete introduction of the parallel strategy used in INCOMPACT3D, refer to Laizet and Li [42]. A detailed description of the DNS code INCOMPACT3D can be found in work by Laizet and Lamballais [40] and also Laizet *et al.* [41].

It is well known that the characteristics of a dual-plane jet flow in the far downstream region resemble those in a turbulent plane jet. Moreover, in free shear flows (e.g., wakes, jets, mix layers), the mean velocity requires the shortest streamwise distance to reach self-similarity (self-preservation) compared with other higher order statistics. Therefore, to validate our simulation the vertical distributions of the normalized mean streamwise velocity $(U - U_A)/(U_C - U_A)$ in the far downstream region at $X/L_0 = 24$, 26, and 28 for the case with $L_d/L_0 = 4$ are compared against previous experimental and numerical studies in Fig. 3. The width $\delta(X)$ in Fig. 3 is defined as the distance between the centerline and the point where $(U - U_A)/(U_C - U_A) = 0.5$ with U_C being the

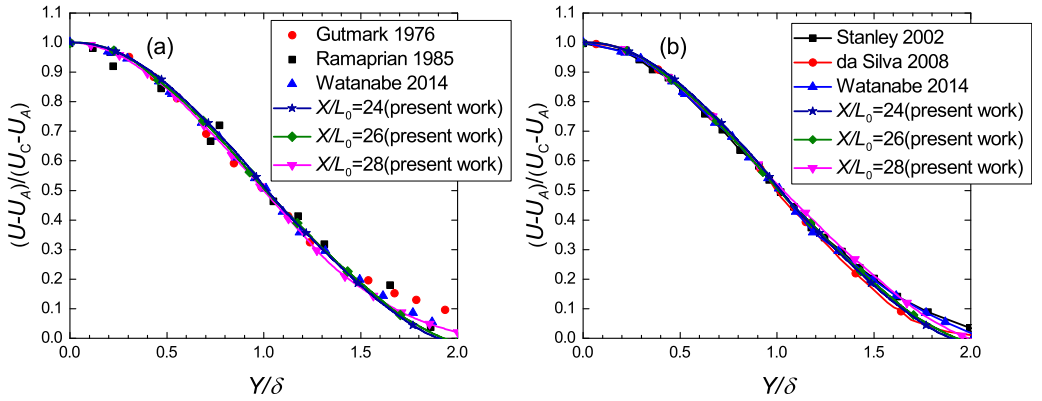

FIG. 3. Comparison of the vertical distribution of the normalized mean streamwise velocity $(U - U_A)/(U_C - U_A)$ at three different downstream locations (i.e., $X/L_0 = 24$, 26, and 28) for the case with $L_d/L_0 = 4$ with previous studies (a) experiments by Gutmark and Wygnansky [46], Ramparian and Chandrasekhara [47], and Watanabe *et al.* [31]. (b) DNSs by Stanley *et al.* [32], da Silva and Pereira [48], and Watanabe *et al.* [31].

mean velocity along the centerline. The good agreement with previous studies at higher Reynolds numbers (e.g., $\mathrm{Re}_{L_0} = 30\,000$ in Gutmark and Wygnansky [46]) gives us more confidence in the results of our simulation. The satisfying collapse with previous numerical and experimental studies also suggests that for the case with $L_d/L_0 = 4$, the lateral domain size L_Y is unlikely to affect the development of the dual-jet flow. Watanabe *et al.* [29] have already demonstrated that for a single planar jet, the ratio $L_Y/\delta \simeq 10$ would be sufficient. However, as can be seen from Fig. 4, for the case $L_d/L_0 = 8$ the two jets have not fully merged at $X/L_0 = 28$ and the maximum U is found at off-centerline positions. Consequently, we cannot directly adopt this criterion. We propose a quasi-half-width b, which is defined as the distance between the centerline and the point where

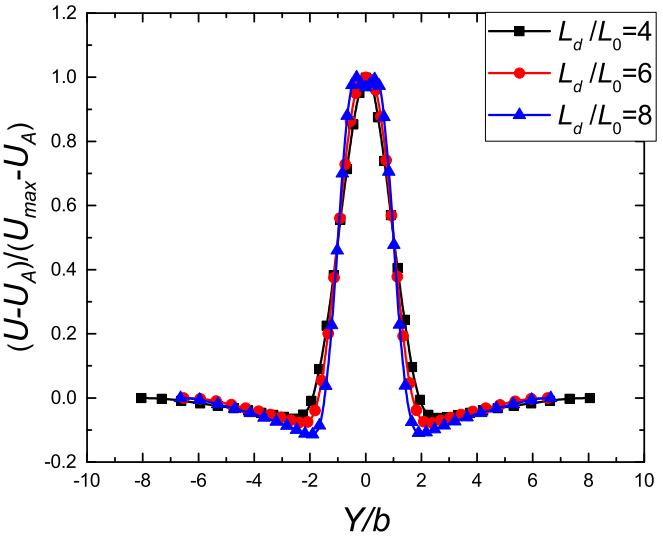

FIG. 4. Vertical distribution of the normalized mean streamwise velocity $(U - U_A)/(U_C - U_{\max})$ at the far downstream location (i.e., $X/L_0 = 28$) for all three cases (i.e., $L_d/L_0 = 4$, 6, and 8). To investigate the influence of the lateral domain, the vertical distribution of U within the range $-L_Y/2 \leqslant Y/L_0 \leqslant L_Y/2$ is plotted.

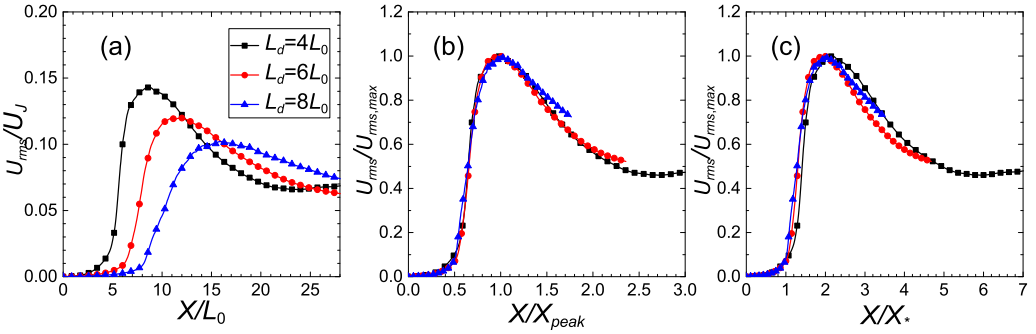

FIG. 5. Streamwise evolution of the streamwise turbulence rms value U_{rms}/U_J vs (a) X/L_0, (b) X/X_{peak}, and (c) X/X_* along the centerline.

$(U - U_A)/(U_{\max} - U_A) = 0.5$ with $U_{\max}$ being the maximum U. Obviously, for the cases with $L_d/L_0 = 4$ and 6, where the $U_{\max}$ is found to be located on the centerline, we have $\delta = b$. Figure 4 shows that for all three cases considered the ratios L_Y/b are larger than 10. It is expected therefore that the vertical sizes L_Y chosen are sufficiently large. Figure 3, somehow, confirms that our choice of the ambient velocity U_A/U_J are not expected to significantly affect the dynamics of the flow field, at least in the downstream region where the combined jet is self-similar for the mean velocity (see Fig. 3).

III. JET-INTERACTION LENGTH SCALE

In a previous study on grid-generated turbulence, Mazellier and Vassilicos [14] proposed the wake-interaction length scale, which is based on the scaling law of a single wake width, to normalize the streamwise distance from the grid bar. In a more recent particle image velocimetry study, Gomes-Fernandes *et al.* [17] investigated the wake-interaction length scale in grid-generated turbulent flow with free-stream turbulence. It has been found that the streamwise evolution of various statistics along the centerline (e.g., mean streamwise velocoity, turbulence intensity, skewness of the streamwise velocity fluctuations, etc.) all scale with the wake-interaction length scale. In other words, once the geometry of the grid is known, the behavior of grid-generated turbulence can be predicted, at least to some extent.

We first drive the jet-interaction length scale X_* and then check whether X_* can predict the spatial evolution of the jet interaction. When considering the streamwise evolution of the characteristics width $\delta(X)$ of a planar jet, we have $\delta(X) \propto X$ [49]. Watanabe *et al.* [30] demonstrated that for a planar jet, the PDFs of the height of turbulent/nonturbulent interface scale with $\delta(X)$ with the averaged interface height $Y_I(X) \simeq 1.43\delta(X)$. We further assume that such relation could still hold in the near field of a dual-plane jet flow. Therefore, the interaction of the turbulent/nonturbulent interface of the two plane jets will happen at a mean streamwise location of interaction X along the centerline, such that $Y_I(X) = (1/2)L_d = 1.43\delta(X) \propto X$. Based on the above assumptions, we can now safely introduce $X_* = L_d$ as the jet-interaction length scale. It should be stressed that the assumptions employed here are quite strong and the deflection movement of the two jets is also neglected. The evolutions of various statistics along the centerline for all three cases are examined below to justify the suitability of the proposed jet-interaction length scale X_*.

Figure 5 shows the centerline turbulence rms value as functions of X/L_0, X/X_{peak}, and X/X_* for all three cases, where X_{peak} is the location of maximum U_{rms}/U_J. A reasonably good collapse can be found in Figs. 5(b) and 5(c), when the downstream distance X is normalized by X_{peak} or X_*. The collapse in Fig. 5(c) reveals that X_* could be a potential candidate to characterize the behavior of jet interaction due to different L_d.

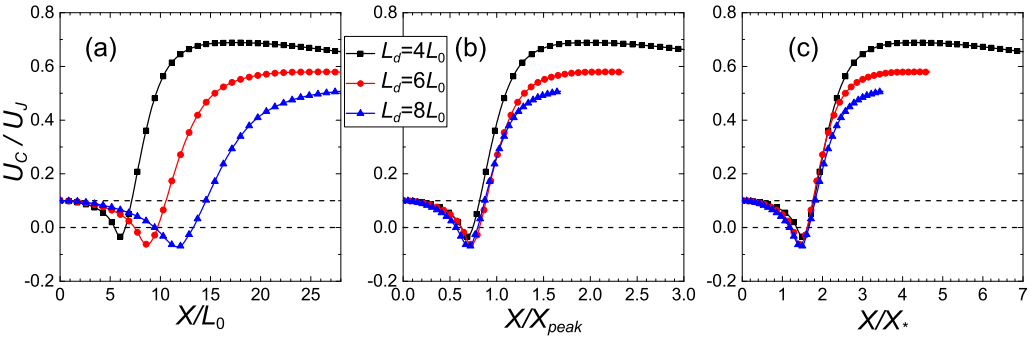

FIG. 6. Streamwise evolution of the mean streamwise velocity U_C/U_J vs (a) X/L_0, (b) X/X_{peak}, and (c) X/X_* along the centerline. The two dashed lines in the three subfigures indicate $U_C/U_J = 0.1$ and 0.0.

In Fig. 6, we plot the streamwise evolution of the mean velocity U_C/U_J along the centerline as functions of X/L_0, X/X_{peak}, and X/X_*. It can be seen from Figs. 6(b) and 6(c) that U_C/U_J appears to collapse in the upstream region. This finding is not trivial because previous study [3] suggested a linear relationship between the streamwise location of the merge point X_{mp} and the separation distance L_d, which is consistent with our simulation result. The merge point X_{mp} is defined as the streamwise location where the mean streamwise velocity U is zero. Also, it is demonstrated that the linear relationship stems from the assumption $Y_I(X) = (1/2)L_d = 1.43\delta(X) \propto X$. It should be stressed that the location X_{mp} is likely to depend on the strength of the coflow (i.e., $U_A/U_J = 0.1$ in current study). Further investigation is required to study the influences of the coflow.

In the further downstream region, however, the profiles of U_C/U_J do not collapse. For a given downstream location normalized by X_* (e.g., $X/X_* = 3$), U_C/U_J is found to have the largest value in the case with $L_d/L_0 = 4$. This is because as L_d decreases, for a given far-downstream location X/X_* (i.e., $X/X_* = 3$ as shown in Fig. 7), the width of the combined-jet in the Y direction becomes narrower, and the corresponding mean streamwise velocity increases.

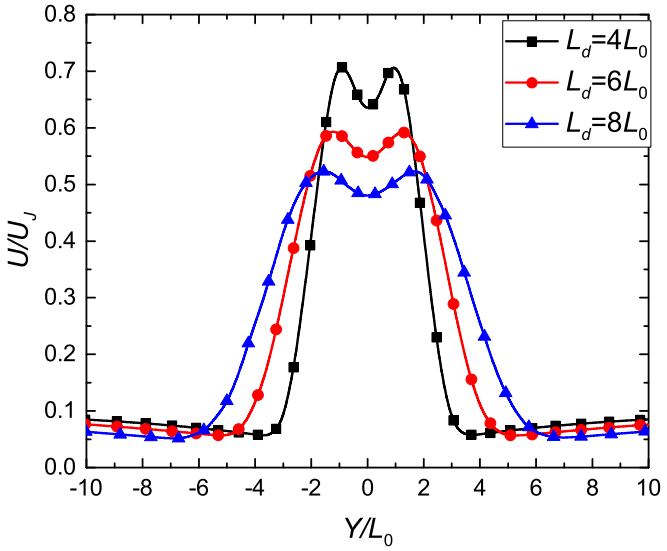

FIG. 7. Vertical distribution of U/U_J at $X/X_* = 3$ for all three cases.

TABLE II. Normalized wake-interaction scale X_*, locations of the merge point X_{mp} and turbulence intensity peak X_{peak}. The ratios normalized by the corresponding values from the case with $L_d/L_0 = 4$ (e.g., $X_{*,1}$, $X_{mp,1}$, and $X_{\text{peak},1}$).

Run	X_*/L_0	$X_*/X_{*,1}$	X_{mp}/L_0	$X_{mp}/X_{mp,1}$	X_{peak}/L_0	$X_{\text{peak}}/X_{\text{peak},1}$
JI4	4.0	1.0	6.5	1.0	8.7	1.0
JI6	6.0	1.5	9.7	1.5	12	1.4
JI8	8.0	2.0	13	2.0	16	1.8

In Table II, the locations of the merge point X_{mp} and turbulence intensity peak X_{peak} for all three cases and the corresponding nondimensional ratios are reported. Table II suggests that X_*, X_{mp}, and X_{peak} can all be used as the characteristic length scale.

To fully investigate the jet interaction due to different L_d and the suitability of X_*, various centerline statistical variables (e.g., the small-scale anisotropy, large-scale anisotropy, skewness, and kurtosis of streamwise velocity fluctuations) are also plotted. As shown in Figs. 8–11, the profiles of the small-scale anisotropy, large-scale anisotropy, skewness, and kurtosis appear to fall on a single line when plotted as a function of X/X_*.

It is clear from Figs. 10 and 11 that for all three cases with different L_d, in the upstream region the distribution of the velocity fluctuations can also be highly non-Gaussian since for a Gaussian distribution, the corresponding skewness and kurtosis are $S_u = 0$ and $F_u = 3$. For all three cases, in the upstream region, the negative S_u and the large kurtosis (i.e., $F_u > 5$) suggest the existence of rare events with $u' < 0$. Figures 10(c) and 11(c) indicate that the evolution of the skewness and the kurtosis along the centerline also appear to scale with the jet-interaction length scale. The good collapses of the centerline statistics in Figs. 8–11 lend indirect support to our choice of the lateral domain size L_Y. In a large-eddy simulation with inlet Reynolds number $\text{Re}_{L_0} = 4000$ by Bisoi *et al.* [50], dual-plane jet flow with a small separation distance $L_d/L_0 = 1$ was studied, which therefore allows a large normalized streamwise extent up to $X/X_* = 50$. It has been demonstrated that at the far downstream locations $X/X_* = 15$, 20, 25, and 30, where the normalized mean streamwise velocity resembles that in a well-developed turbulent plane jet, the corresponding skewness values of u' are negative, which actually echoes our current observation of the case with $L_d/L_0 = 4$ [see Fig. 10(c)]; that is, non-Gaussian distribution of velocity fluctuations can indeed be found in turbulence generated by jet interactions. Their flatness at $X/X_* = 15$, 20, 25, and 30, however, are different from our current study. Here, for instance, at $X/X_* = 7$ for the case with $L_d/L_0 = 4$, F_u is larger than 3 [see Fig. 11(c)], whereas in Bisoi *et al.* [50], the corresponding

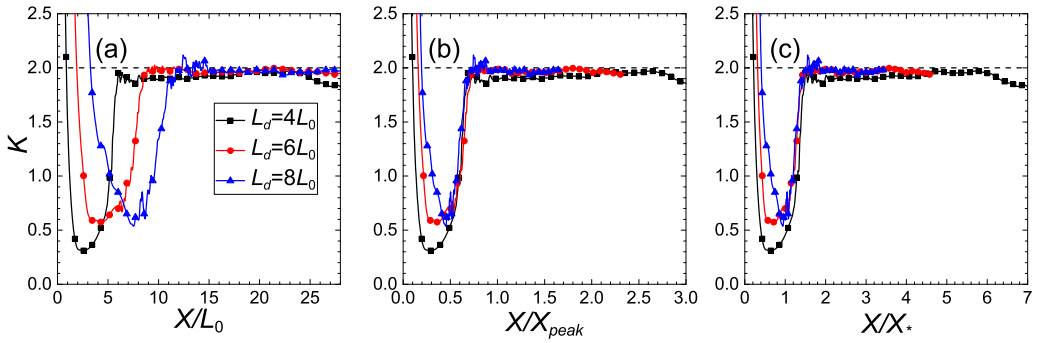

FIG. 8. Evolution of the small-scale anisotropy $K = \langle(\partial v'/\partial x)^2\rangle/\langle(\partial u'/\partial x)^2\rangle$ with $\langle\rangle$ denoted as the ensemble average over time and Z. K vs (a) X/L_0, (b) X/X_{peak}, and (c) X/X_* along the centerline. The horizontal dashed lines indicate $K = 2$.

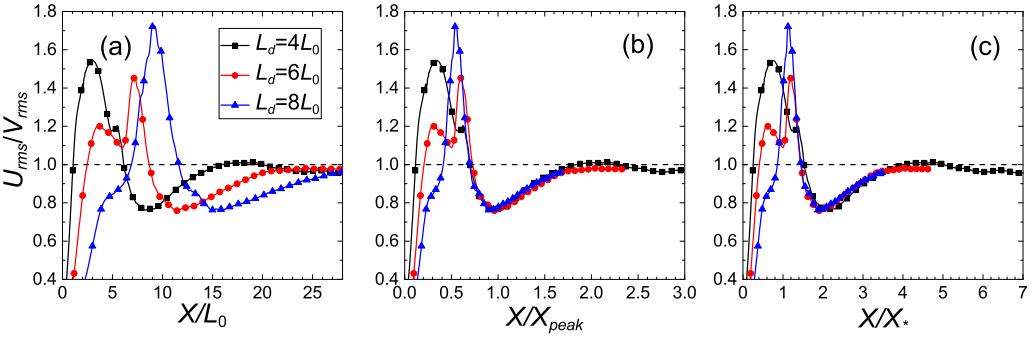

FIG. 9. Streamwise evolution of the large-scale anisotropy U_{rms}/V_{rms} vs (a) X/L_0, (b) X/X_{peak}, and (c) X/X_* along the centerline. The horizontal dashed lines indicate $U_{rms}/V_{rms} = 1$.

F_u at $X/X_* = 15, 20, 25,$ and 30 are slightly less than 3. It might be worth mentioning that in this study the jet interactions in the upstream region (i.e., $X/X_* \leqslant 4$) are of particular interest, whereas in Bisoi *et al.* [50] the turbulence characteristics at considerably far downstream locations (i.e., $X/X_* = 15, 20, 25,$ and 30) are extensively studied. In the following subsections, we will explore the physical mechanism that would cause the non-Gaussian distribution along with the non-Gaussian distribution of u' itself. In an experimental investigation [51] of dual-wake interactions with much larger separation distances (i.e., $L_d/L_0 = 30$ and 40), linear relationship between the streamwise locations of the merge points and separation length has also been reported (see Table 1 in Lin and Sheu [51]), although no further physical explanation was given. Moreover, the locations of the merge points also scale with X_* (see Table 2 in Lin and Sheu [51]). This observation suggests from the scaling behavior that the evolution of dual-jet flow scales with the jet-interaction length scale X_* seems to be valid even for a much larger separation length (i.e., $L_d/L_0 = 30$ and 40).

Figure 12 demonstrates that profiles of the centerline mean pressure also appear to collapse together based on X_{peak} or X_*. A similar experimental observation was already made by Marsters [52], although in the experiment the evolution of centerline static pressure was presented and there is an angle between jet axis and system centerline. A detailed discussion of the streamwise evolution of centerline mean pressure for the case $L_d/L_0 = 6$ will be given later.

In this subsection, we demonstrated that for all three cases the streamwise evolution of various centerline statistics scale with X_*, X_{mp}, and X_{peak}. This finding opens an avenue for the study of jet interaction, although strong assumptions are made to derive X_*. If an appropriate length scale (X_*, X_{mp}, or X_{peak} in this DNS study) is used to normalize the downstream distance X, the evolution

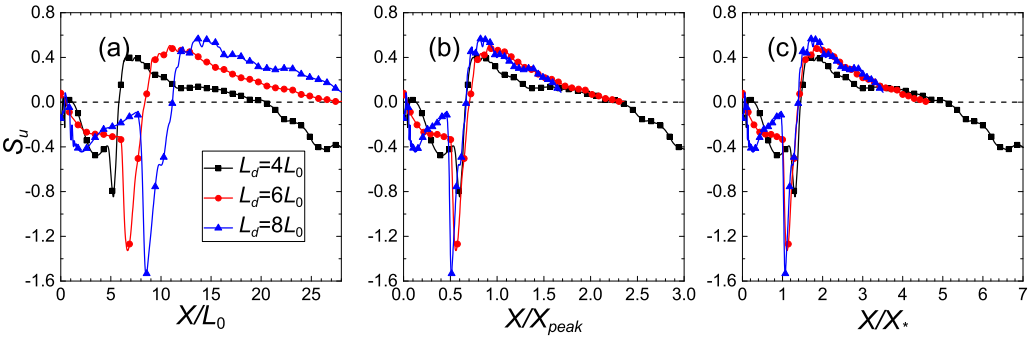

FIG. 10. Streamwise evolution of the skewness of the streamwise velocity fluctuations $S_u = \langle u'^3\rangle/\langle u'^2\rangle^{3/2}$ vs (a) X/L_0, (b) X/X_{peak}, and (c) X/X_* along the centerline. The horizontal dashed lines indicate $S_u = 0$.

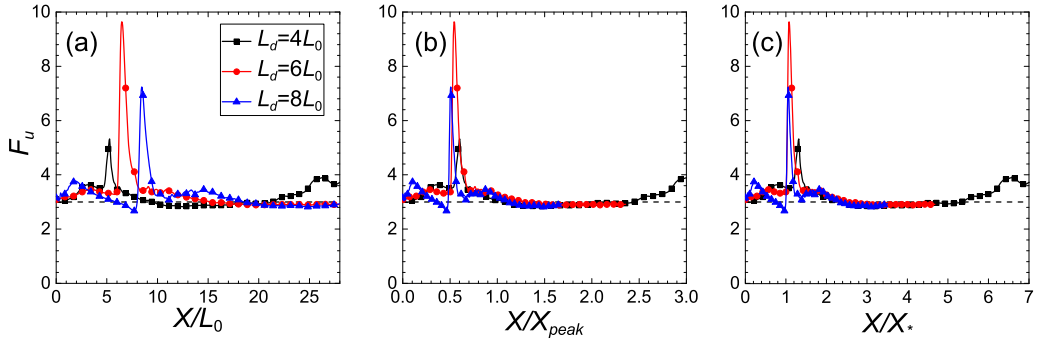

FIG. 11. Streamwise evolution of the kurtosis of the streamwise velocity fluctuations $F_u = \langle u'^4\rangle/\langle u'^2\rangle^2$ vs (a) X/L_0, (b) $X/X_{\rm peak}$, and (c) X/X_* along the centerline. The horizontal dashed lines indicate $F_u = 3$.

of turbulence characteristics in jet interaction with different L_d follows a similar pattern. Thus, in the following subsections only detailed investigations on the case with $L_d/L_0 = 6$ are presented for economy of space. Before closing this subsection, we emphasize that the jet-interaction length scale X_* is quite different from the merge point X_{mp}; the jet-interaction length scale X_* is derived from the development of a single jet, whereas the location of the merge point X_{mp} is directly related to the existence of the reversal flow, which is caused by a superatmospheric region with positive pressure, as shall be shown in the following subsections.

IV. FLOW PROPERTIES AND VELOCITY FLUCTUATIONS

A. Flow visualisations

In Fig. 13, we plot the instantaneous vorticity magnitude $\Omega/(U_J/L_0)$ in the X-Y plane at $Z = 0$ for the case with $L_d/L_0 = 6$. The vorticity is defined as $\Omega = (\Omega_i\Omega_i)^{(1/2)}$, where $\Omega_i = \varepsilon_{ijk}\partial u_k/\partial X_J$ and ε_{ijk} denotes the Levi-Civita symbol. It can be seen that the two jets are deflected toward each other and joint together at $X/L_0 \simeq 8$. Beyond this location, the two plane jets gradually grows into a single jet owing to turbulent mixing. As the fluid particles in the initial region surrounded by the two jets become entrained into the two inner turbulent layers, a subatmospheric pressure zone with negative pressure can be formed. Because of the subatmospheric pressure region, the two jets are deflected toward each other (for a clear demonstration, see Fig. 14). It is worth mentioning that in the nonturbulent regions (i.e., both regions surrounded by the two jets and outside the dual-plane jet flow) close to the exits of two plane jets, for example, at $X/L_0 \simeq 2$, the deflection of the streamlines

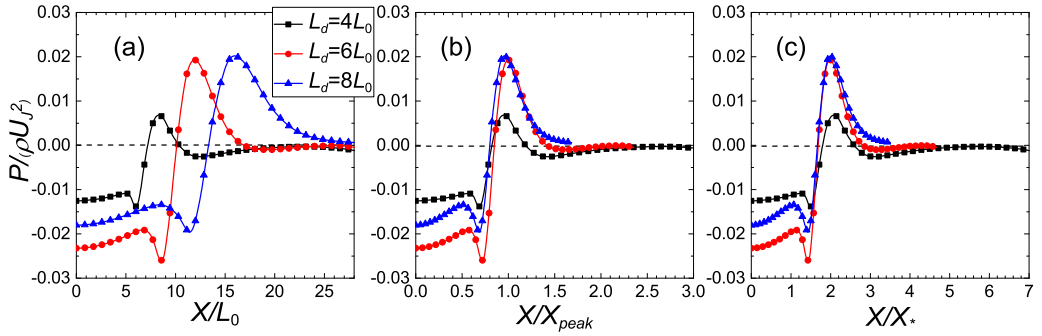

FIG. 12. Streamwise evolution of the normalized mean pressure $P/(\rho U_J^2)$ vs (a) X/L_0, (b) $X/X_{\rm peak}$, and (c) X/X_* along the centerline. The horizontal dashed lines indicate $P = 0$.

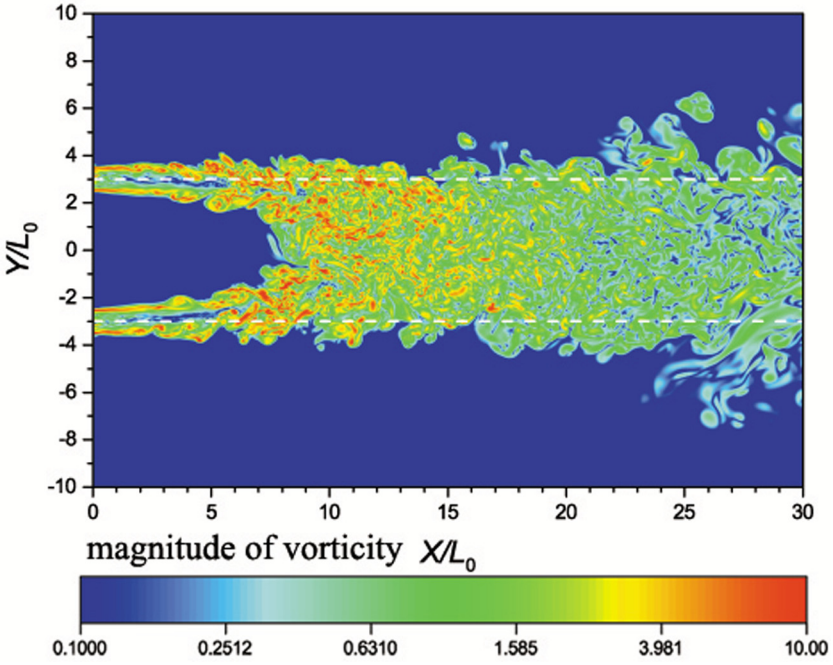

FIG. 13. Magnitude of instantaneous vorticity field $\Omega/(U_J/L_0)$ in the X-Y plane for the case with $L_d/L_0 = 6$. This visualization is in the region $-10 \leqslant Y/L_0 \leqslant 10$ at $Z/L_0 = 0$ covering only 50% of the simulation domain. The two horizontal lines indicate the centerlines of the jet exits.

appears to be closely related to the entrainment process. Thus, from the statistical point of view, two different but closely related transverse movements can be identified in the upstream regions (i.e., $X/L_0 \leqslant 8$); one is the entrainment movement of the fluid particle in the above-mentioned nonturbulent region and the other is the deflection movement of the two jets.

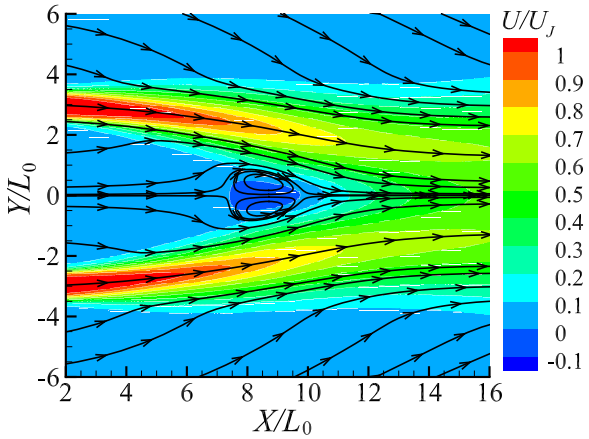

FIG. 14. Mean streamlines in the vicinity of the jet exits for the case with $L_d/L_0 = 6$. The color contours correspond to the normalized mean streamwise velocity U/U_J. This visualization is in the region $2 \leqslant X/L_0 \leqslant 16$ and $-6 \leqslant Y/L_0 \leqslant 6$.

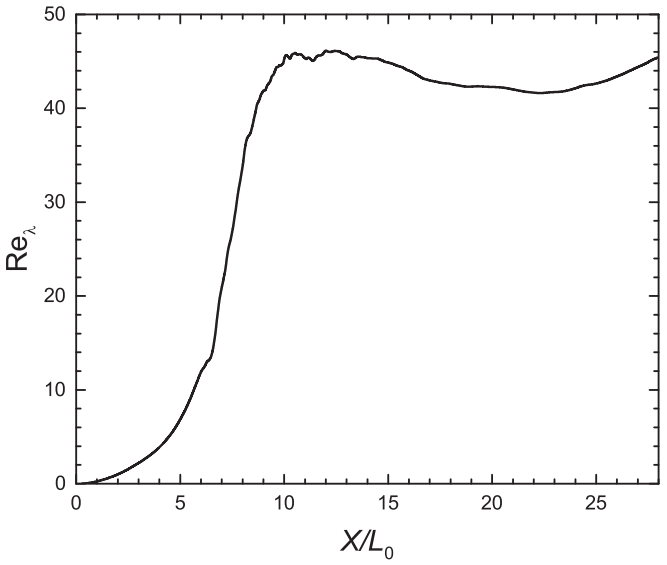

FIG. 15. Streamwise evolution of the local Reynolds number based on the Taylor microscale along the centerline for the case with $L_d/L_0 = 6$.

The mean streamwise velocity and the mean streamlines in the region $2 \leqslant X/L_0 \leqslant 16$ and $-6 \leqslant Y/L_0 \leqslant 6$ for the case with $L_d/L_0 = 6$ are shown in Fig. 14. Two contrarotary vortices can be identified just upstream of the joint point (i.e., $X/L_0 \simeq 12$). The existence of recirculation vortices has already been reported in previous experimental studies [4–6]. In the following sections, we will go one step further to provide a more complete picture of the recirculation vortices.

B. Centerline statistics and large-scale movement

Because of the existence of two contrarotary vortices (see Fig. 14), a reversal flow zone can be found at approximately $7 \leqslant X/L_0 \leqslant 10$ (see Fig. 6). In previous studies [4–6], the location $X/L_0 \simeq 10$, where U is zero, is often referred to as the merge point. Because of the jet interactions, the value of U_{rms}/U_J progressively increases with streamwise distance and reaches a peak value at $X_{\text{peak}} \simeq 12L_0$ (see Fig. 5). The streamwise evolution of the local Reynolds number $\text{Re}_\lambda (=\lambda u_{rms}/\nu)$ along the centerline for the case with $L_d/L_0 = 6$ is presented in Fig. 15, where the Taylor microscale λ is defined as $\sqrt{\langle u'^2\rangle/\langle(\partial u'/\partial x)^2\rangle}$ with u' being the instantaneous streamwise velocity fluctuation. After the intensity peak location X_{peak}, U_{rms}/U_J starts to decrease and the local Reynolds number is around 45.

The streamwise evolution of the mean pressure P normalized by the inlet velocity U_J and flow density ρ along the centerline for the case with $L_d/L_0 = 6$ is plotted in Fig. 16. A subatmospheric pressure region (with negative pressure) can be found in the region $X/L_0 \leqslant 10$. And due to jet interactions, the pressure increases rapidly and consequently a superatmospheric pressure region (with positive pressure) is formed. As suggested in previous studies [4–6], this superatmospheric region is responsible for the reversal flow shown in Fig. 6(a). The pressure takes small negative values downstream of the superatmospheric region and then gradually rises to the atmospheric value. This subtle variation is also reported in previous experiments by Tanaka [6] and Marsters [6], lending credence to our present simulation.

Figure 16 also indicates that the mean pressure profile possesses two peaks located at $X/L_0 \simeq 7$ and $X/L_0 \simeq 12$, respectively. Considering the mean velocity distribution [see Fig. 6(a)], it can be seen that the first peak is close to the location of zero velocity value. It is well known that in the

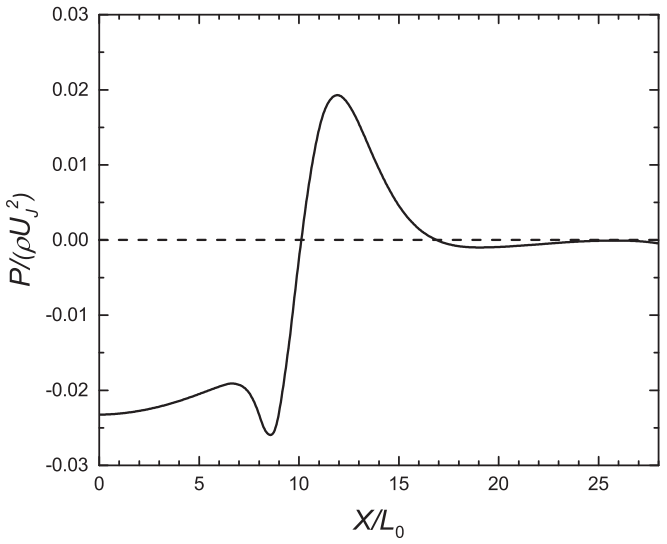

FIG. 16. Streamwise evolution of the normalized mean pressure $P/(\rho U_J^2)$ along the centerline for the case with $L_d/L_0 = 6$.

case of flow past a solid body, high pressure can be found on the front face of the solid body. The high-pressure peak found here is introduced by the quasistagnation behavior imposed by the two contrarotary vortices instead of a solid body. The second pressure peak is at $X/L_0 \simeq 12$, where the turbulence intensity also reaches its maximum value. Thus, this pressure peak is associated with direct jet interactions.

It is well known that at a sufficiently large Reynolds number, the small-scale turbulence is locally isotropic and K equals to 2. The small-scale turbulence becomes locally isotropic at $X/L_0 \geqslant 9$ (see Fig. 8). As shown in Fig. 9, the large-scale anisotropy U_{rms}/V_{rms} can persist for a much longer time when compared against the evolution of the small-scale anisotropy K. Only at $X/L_0 \geqslant 20$, the value of U_{rms}/V_{rms} is close to 1. For instance, at $X/L_0 = 12$, small-scale isotropy can be fully achieved, while the large-scale anisotropy is still significant. This observation is in accord with the Kolmogorov's local isotropy assertion, although the local Reynolds number is quite small (see Fig. 15).

In the case of jet interactions, in the upstream region the distribution of the velocity fluctuations can also be non-Gaussian. With increasing downstream distance, S_u gradually evolves to the corresponding values of a Gaussian distribution [i.e., $S_u \simeq 0$ at $X/L_0 = 25$; see Fig. 10(a)]. One interesting finding is that close to the inlet (i.e., $X/L_0 \leqslant 9$), even without direct interactions of the inner shear layers, the non-Gaussian distribution of velocity fluctuations can also be found.

To investigate the streamwise evolution of turbulent motions, we select three different streamwise locations (i.e., $X/L_0 = 7$, 12, and 25) corresponding to the large negative, large positive, and near-zero values of S_u. The PDFs of the normalized streamwise velocity fluctuation u'/U_{rms} at the three locations considered are shown in Fig. 17 to obtain a complete picture. The skewness directly reflects a distribution's asymmetry, whereas the kurtosis describes the extent to which the distribution is fat tailed or light tailed. The zero value of S_u does not necessary validate a Gaussian distribution. Our first finding is that at $X/L_0 = 7$, the distribution is negatively skewed and the probability of the occurrence of the large negative streamwise velocity fluctuations is much higher than the corresponding Gaussian distribution. Albeit describable positively skewed, the general shape of $P(u')$ at $X/L_0 = 12$ resembles that at the far downstream location $X/L_0 = 25$, where the fluctuations u' acquire a near Gaussian distribution.

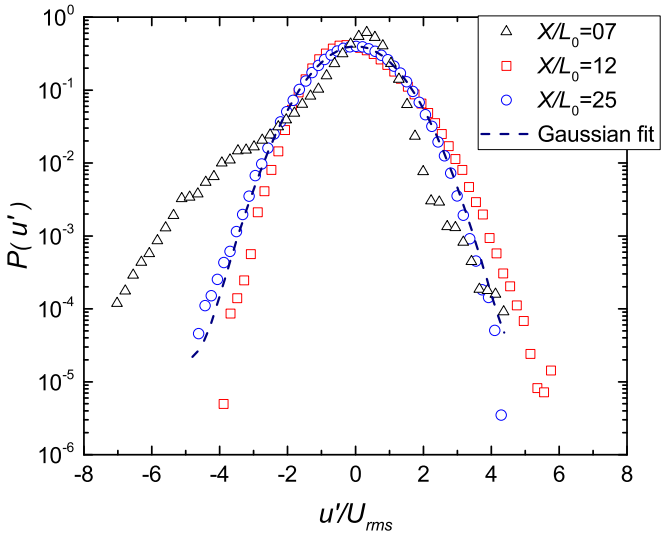

FIG. 17. PDFs of the normalized streamwise velocity fluctuation u'/u_{rms} at $X/L_0 = 7$, 12, and 25. The Gaussian fit of $P(u')$ at $X/L_0 = 25$ is also shown for comparison.

We also plot the traces of the streamwise velocity fluctuation versus time in Fig. 18. Note that the time traces are collected from the same time step. At $X/L_0 = 7$, compared with the downstream locations, the variation of the fluctuating streamwise velocity component u' is much slower. Figure 19(a) shows that at $X/L_0 = 7$ the existence of the negative skewness is closely related to the relatively larger magnitude of vorticity. Moreover, the flow at $X/L_0 = 7$ is intermittent; alternation between the nonturbulent region (i.e., $\Omega \simeq 0$) and the turbulent region with non-negligible magnitude of Ω can be identified.

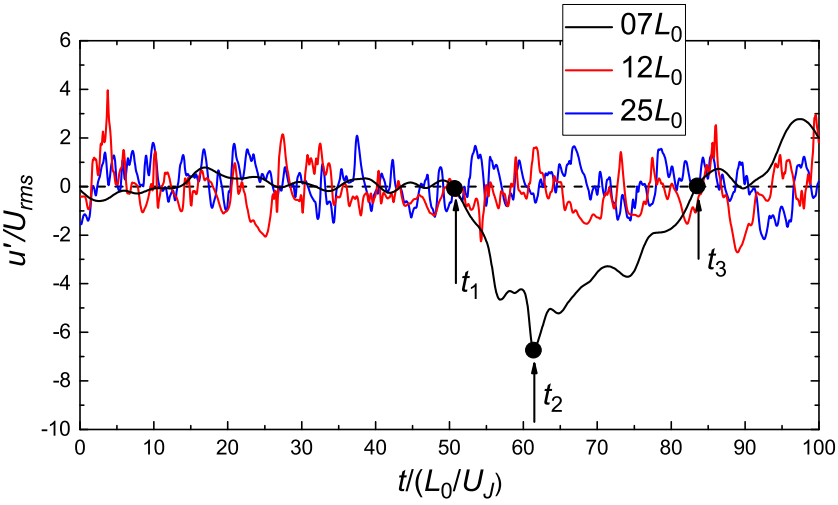

FIG. 18. Normalized fluctuating streamwise velocity component at $X/L_0 = 7$, 12, and 25 for the case with $L_d/L_0 = 6$. The filled circle symbols represent the selected three times at the streamwise location $X/L_0 = 7$ with $t_1/(L_0/U_J) = 50.7$, $t_2/(L_0/U_J) = 61.3$, and $t_3/(L_0/U_J) = 83.5$. The horizontal dashed line corresponds to $u'/U_{rms} = 0$.

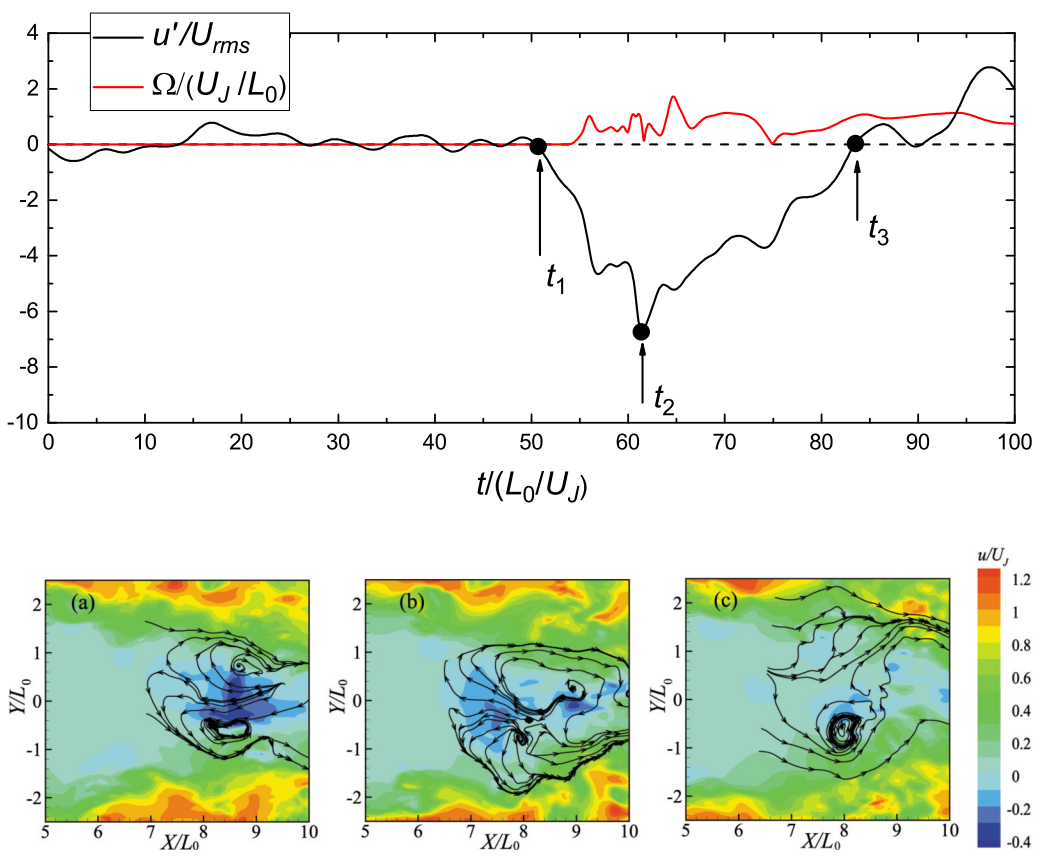

FIG. 19. (Top) Normalized fluctuating streamwise velocity component u' and the magnitude of vorticity Ω at $X/L_0 = 7$ and for the case with $L_d/L_0 = 6$. The horizontal dashed line represents $u' = 0$ and $\Omega = 0$. The same filled circle symbols plotted in Fig. 18 are also included. (Bottom) Instantaneous streamwise velocity field and the streamlines in the reverse flow region in the X-Y plane for the case with $L_d/L_0 = 6$. From left to right, subfigures (a), (b), and (c) are plotted in the sequence of time t_1, t_2, and t_3. To highlight the existence of recirculation vortices, only the streamlines corresponding to large negative u are drawn.

We select three different time shots [see Figs. 19(a) and 19(b)] to further study the slower variation of u' at $X/L_0 = 7$. The instantaneous streamwise velocity field and the corresponding streamlines are plotted in Fig. 19. For all three time shots, reversal flows and the resulting contrarotary vortices can be observed. It can be seen that the reversal flow region with largest negative u' at $X/L_0 = 7$ (also at time shot t_2) is found at the most upstream location [see Fig. 19(b)]. It has been demonstrated here and in previous studies [4–6] that the reversal flow (i.e., contrarotary vortices) can be driven by the downstream higher pressure region; the high-pressure region at the downstream location would drive the fluid particles travel toward the inlet. Hence, the slow deviation from the mean value at the quasistagnation point (i.e., $X/L_0 = 7$), where U equals to zero, find its roots in the large-scale movement of the contrarotary vortices, which is directly caused by the feedback of the pressure from the downstream region.

To take the observation in Fig. 19(a) (that the flow at $X/L_0 = 7$ is intermittent) one step further and quantitatively describe large-scale movement of the contrarotary vortices, the intermittency factor γ is examined. The intermittency factor γ is defined as the fraction of time that fluid points are in the turbulent region. For a shear flow, it contains two regions (turbulent region and nonturbulent

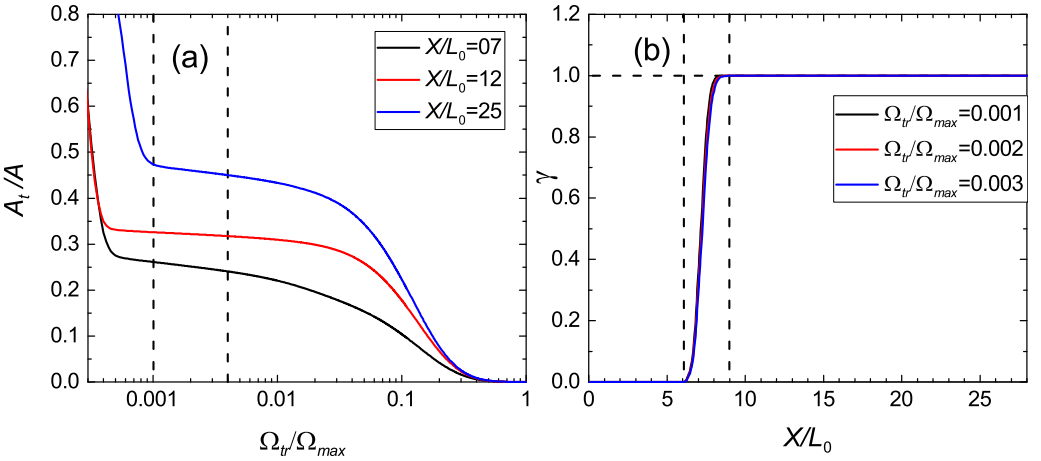

FIG. 20. (a) Time-averaged area fraction of turbulent region at $X/L_0 = 7$, 12, and 25. The two vertical dashed lines (i.e., $\Omega_{tr}/\Omega_{\max} = 0.001$ and 0.003) show the range within which for all three cases plateaus of A_t/A exist. (b) Streamwise evolution of γ along the centerline under three different thresholds. The horizontal dashed line represents fully turbulent state (i.e., $\gamma = 1.0$). The two vertical dashed lines (i.e., $X/L_0 = 6$ and 9) define the intermittent region.

region), which are separately by the turbulent/nonturbulent interfaces. For a point which is always located in the turbulent region, $\gamma \simeq 1$. In contrast, for a point which is outside of the turbulent region and far away from the turbulent/nonturbulent interface, the value of γ is expected to be zero.

Before computing γ, at first we need to determine the threshold Ω_{tr}, through which the turbulent/nonturbulent interfaces can be accurately captured. In this work, the algorithm proposed by Zhou and Vassilicos [53] is adopted, which is quite similar to the method used by Watanabe *et al.* [29–31] and Taveira *et al.* [54]. Figure 20(a) shows the time-averaged ratio of the turbulent region A_t to the whole simulated area A as a function of $\Omega_{tr}/\Omega_{\max}$, where A_t corresponds to the area of the turbulent region where the normalized magnitude of local vorticity $\Omega/\Omega_{\max}$ is larger than $\Omega_{tr}/\Omega_{\max}$, and $\Omega_{\max}$ is the maximum magnitude of Ω at time t in the Y-Z plane considered. As shown in Fig. 20(a), plateaus can be identified in the range of $0.001 \leqslant \Omega_{tr}/\Omega_{\max} \leqslant 0.003$ for all three location considered. It is believed that if using the vorticity magnitude within the range of $0.001 \leqslant \Omega_{tr}/\Omega_{\max} \leqslant 0.003$ to detect the turbulent/nonturbulent interface, we would have quite similar descriptions of the statistics based on locations of turbulent/nonturbulent interfaces.

Figure 20(b) demonstrates that the distribution of intermittency factor γ is independent of the threshold chosen. Therefore, the threshold within the range $0.001 \leqslant \Omega_{tr}/\Omega_{\max} \leqslant 0.003$ could be used to define the turbulent/nonturbulent interfaces. In the upstream region (i.e., $X/L_0 < 6$), the coflow is still strong. Thus, the flow is fully irrotational and the large-scale movement, which is closely associated with large magnitude of Ω, does not occur. Within the subsequent narrow streamwise region, i.e., $6 \leqslant X/L_0 \leqslant 9$, the flow is intermittent and γ increases rapidly. In this region, the skewness of u' acquires negative values, which again demonstrates that the movement associated with the negatively skewed probability distribution of u' can be intermittent. Another finding is that at $X/L_0 = 7$, the corresponding γ is only 0.1. To some extent, the oscillation movements shown in Fig. 19 can be viewed as quasilaminar. Downstream of the location $X/L_0 = 9$, the dual-plane jet flow is always turbulent along the centerline. It is demonstrated that only when the flow is fully turbulent will the small-scale turbulence become locally isotropic [i.e., $K \simeq 2$ as shown in Fig. 8(a)]. A less obvious implication is that the junction of the two jets is expected to be stable since at $X/L_0 = 12$ the value of γ is always 1.

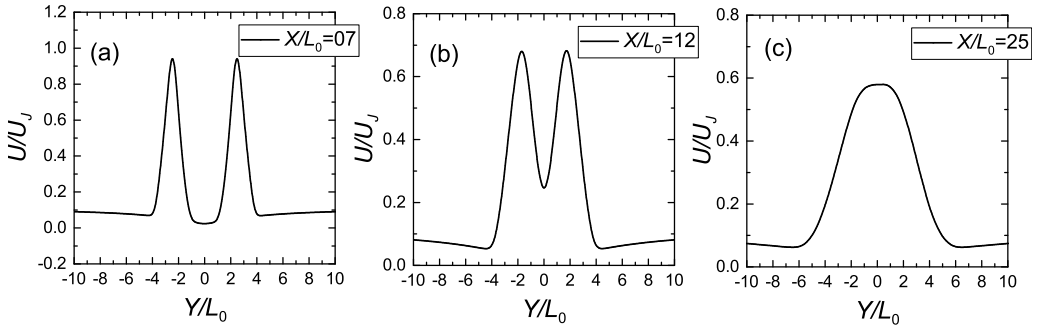

FIG. 21. Vertical distribution of the normalized mean streamwise velocity U/U_J at three different streamwise locations, (a) $X/L_0 = 7$, (b) $X/L_0 = 12$, and (c) $X/L_0 = 25$, for the case with $L_d/L_0 = 6$.

C. Vertical statistics

Figure 21 shows the vertical profiles of the normalized mean streamwise velocity U/U_J at the three chosen locations for the case with $L_d/L_0 = 6$. In the upstream region (i.e., $X/L_0 = 7$ and 12), it is demonstrated that the maximum values of U/U_J are found at $Y/L_0 \simeq \pm 2$ and around the centerline (i.e., $Y/L_0 \simeq 0$) the magnitudes of U/U_J are quite small, indicating that the imprints of the two imposed parallel jets still exist. The flat distribution of U at $X/L_0 = 7$ in the range $-2 \leqslant Y/L_0 \leqslant 2$ reveals that two jets have not yet merged together. In contrast, such a plateau cannot be observed at $X/L_0 = 12$. This variation reveals that the two inner shear layers can intensively directly meet each other at $X/L_0 = 12$. As shown in Fig. 13, at a further downstream location (i.e., $X/L_0 = 25$), the two parallel jets have already fully merged. Thus, the corresponding mean profile seems to acquire the desired shape of a single jet [see Fig. 21(c)].

Figure 22 shows the vertical profiles of the normalized mean vertical velocity V/U_J for the case with $L_d/L_0 = 6$. It can be seen that at different streamwise locations, the general shapes of the profiles of V/U_J are quite different. As shown in Fig. 22(a), at $X/L_0 = 7$, fluid particles in the vertical range $-2 \lesssim Y/L_0 \lesssim 2$ tend to escape from the centerline. This behavior is related to the entrainment processes, in which the particles are entrained into the inner shear layers. In contrast, Fig. 22(b) suggests that fluid particles at $X/L_0 = 12$ move toward the centerline. Because of the deflection and growth of the two jets, the nonturbulent region no longer exists at $X/L_0 = 12$ (see Fig. 20). In other words, the two jets directly interact with each other and the entrainment processes at the centerline side do not occur. Finally, the outward movement at $X/L_0 = 25$ shown in Fig. 22(c) is related to the spread of the jet. Figure 22 also indicates that the mean transverse movement around $Y/L_0 = \pm 2$ at the far-downstream location $X/L_0 = 25$ is much weaker; V/U_J is about an order of magnitude smaller than the corresponding values at the two upstream locations.

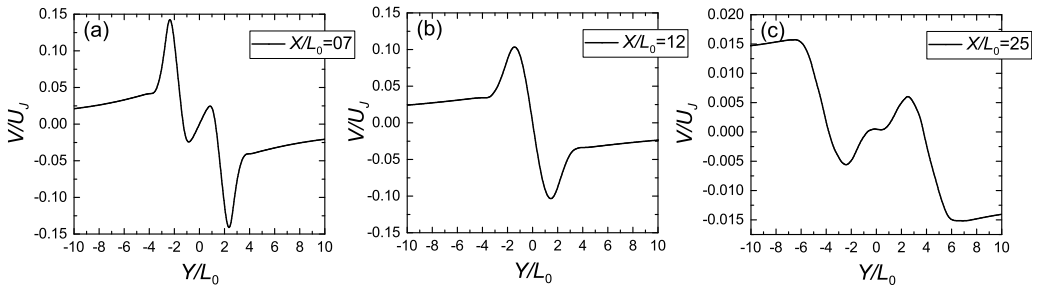

FIG. 22. Vertical distribution of the normalized mean vertical velocity V/U_J at three different streamwise locations, (a) $X/L_0 = 7$, (b) $X/L_0 = 12$, and (c) $X/L_0 = 25$, for the case with $L_d/L_0 = 6$.

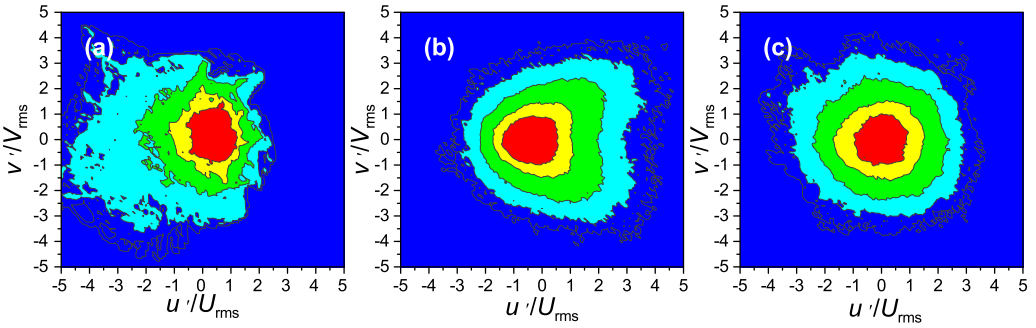

FIG. 23. Joint PDFs of u'/U_{rms} and v'/V_{rms} at three different streamwise locations (a) $X/L_0 = 7$, (b) $X/L_0 = 12$, and (c) $X/L_0 = 25$ for the case with $L_d/L_0 = 6$. The contour levels are 0.1, 0.05, 10^{-2}, 10^{-3}, and 10^{-4}.

In summary, depending on the streamwise distance from the inlet, different flow patterns can be found. For example, at $X/L_0 = 7$, the two jets have not yet merged together and the surrounded region is intermittent, whereas downstream of the merge point, for instance, at $X/L_0 = 12$, direct junctions of the two jets occur.

D. Joint PDFs of u' and v'

In Fig. 23, we plot the joint PDFs of the streamwise and vertical fluctuations u' and v' at $X/L_0 =$ 7, 12, and 25 for the case with $L_d/L_0 = 6$. As expected, the contour lines at all three locations are symmetrical with respect to the horizontal line $v'/V_{rms} = 0$. At $X/L_0 = 7$, the contour lines of the joint PDFs are negatively skewed. Interestingly, the contour lines exhibit a "heart" shape instead at $X/L_0 = 12$. In other words, Fig. 23(b) implies that the intense positive values of u' tend to be associated with the large magnitudes of v'.

From a Lagrangian point of view, one can imagine how the local fluid particles along the centerline can be dramatically accelerated when the two jets traveling toward the centerline (for instance, see the deflection movement shown in Fig. 14). In case of the presence of large magnitude of v', the fluid points along the centerline have a better chance to be from a further transverse location away from the centerline. Figure 21(b) clearly demonstrates that owing to the imprints of the initial conditions, the mean streamwise velocity U around the centerline (e.g., $Y/L_0 = \pm 2$) is significantly larger than the corresponding values along the centerline. If traveling toward the centerline, these faster fluid particles can easily accelerate the local turbulent flow. Depending on the direction of the transverse movement, the streamwise and vertical fluctuations can be either in phase or out of phase with each other (see Fig. 24).

At $X/L_0 = 25$, the contour lines of the joint PDFs acquire a "pizza" shape, implying the mechanism found at $X/L_0 = 12$ no longer exists. This is because with increasing downstream distance, the variation of U in the Y direction is much weaker [see Fig. 21(c)] and moreover, the vertical movement is one order of magnitude smaller when compared with the upstream location $X/L_0 = 12$. Hence, the corresponding distribution of the fluctuations u' is almost Gaussian. The "pizza" shape indicates that at $X/L_0 = 25$ for the contour levels plotted, u' and v' are essentially statistically uncorrelated.

Before closing this subsection, it should be stressed that in the case of grid-generated turbulence, only non-Gaussian distribution of the fluctuations u' with negative skewness can be found and it was also shown that the streamwise location with the largest negative skewness is quite different from the peak intensity location [23–27]. In this study, however, both negatively skewed and positively skewed probability distributions exist and the turbulence intensity peak location is almost the same as the location where the largest positive skewness is taken. Moreover, in grid-generated turbulence

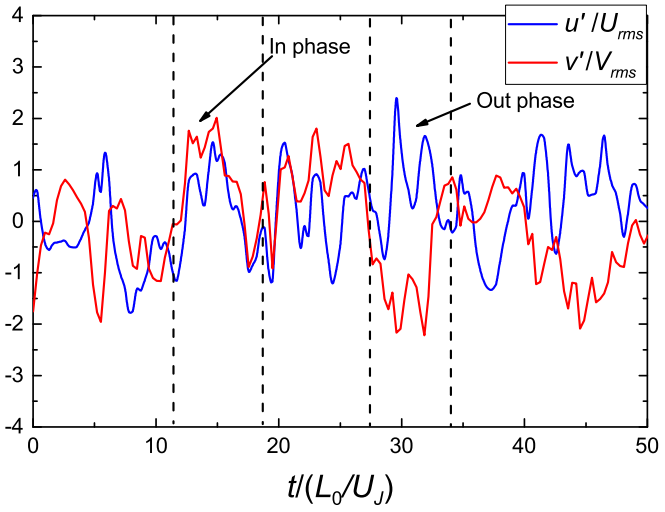

FIG. 24. Time traces of the normalized fluctuating streamwise and vertical velocity components at $X/L_0 = 12$ for the case with $L_d/L_0 = 6$. The two ranges defined by vertical dashed lines clearly imply that u' and v' can be either in phase or out of phase with each other.

except in the vicinity of grid bars, the reversal flow cannot be found anywhere else. Hence, further comparisons between the two different flows should be made in the future work.

E. Energy spectra and small-scale intermittency

We now calculate the one-dimensional energy spectra at three different streamwise locations [$X/L_0 = 7$, 12, and 25; see transparent profiles in Fig. 25(a)], at which the turbulence characteristics have already been extensively discussed in the above sections. The frequency spectra are computed by the Fourier transform of the fluctuation signals at three locations considered. A Savitzky-Golay smoothing filter is applied to the spectra in Fig. 25(a) with the size of the filter

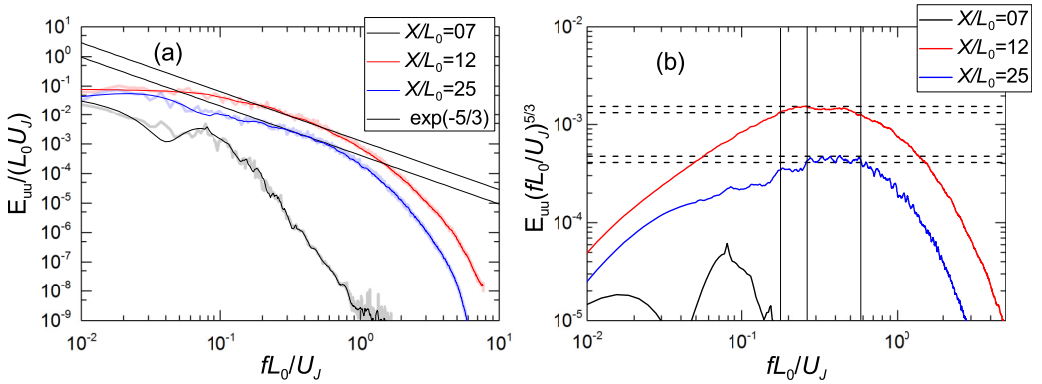

FIG. 25. (a) Energy spectra of the streamwise velocity fluctuations at $X/L_0 = 7$, 12, and 25 for the case with $L_d/L_0 = 6$. The transparent profiles correspond to the original spectra and the opaque profiles correspond to the smoothed spectra and (b) the smoothed compensated energy spectra. The vertical lines describe the ranges of the $-5/3$ scaling. The two horizontal dashed lines represent deviations of -7.5% and 7.5%, respectively, from the mean value.

window being $0.0942 f L_0/U_J$. Consequently, smooth distributions of energy spectra, which allow a more quantitative discussion, can be obtained but at a price: Some frequency details are lost [see opaque profiles in Fig. 25(a)].

The first finding in Fig. 25(a) is that the spectrum profile at $X/L_0 = 7$ exhibits discernible peaks at the normalized frequency $f L_0/U_J \simeq 0.07$. These frequency peaks at $0.06 \leqslant f L_0/U_J \leqslant 0.1$ appear to be associated with the small-scale laminar oscillation movement [as shown in Fig. 19 at $t/(L_0/U_J) < t_1$]. At $X/L_0 = 12$, in contrast, the large-scale motions disappear. This observation is in agreement with our previous suggestion that the jet junction could be rather stable.

It can be also seen from Fig. 25(a) that the energy spectrum at $X/L_0 = 12$ appears to acquire the $-5/3$ power law with the range for approximate half a decade. Note that the local Reynolds number at $X/L_0 = 12$ is only 45 (see Fig. 15). The so-called inertial subrange with a $-5/3$ power-law slope stems from Kolmogorov's second similarity hypothesis, which only applies to turbulent flows at large Reynolds numbers. With increasing downstream distance at $X/L_0 = 25$, even the local Reynolds number remains roughly constant, the flow becomes more homogeneous, and the range of the $-5/3$ slope seems to be eroded.

In Fig. 25(b), the smoothed compensated energy spectra are plotted, as it allows us to quantitatively explore the variation of the $-5/3$ power law. The two horizontal dashed lines represent deviations of -7.5% and 7.5%, respectively, from the mean value. Note that the selected criterion is more demanding than that described by Gomes-Fernandes *et al.* [18] (see Fig. 22 and their allowed deviations are 18% and 16%). Figure 25(b) further verifies that the spectra at $X/L_0 = 12$ and 25 indeed possess a $-5/3$ power-law scaling. And the erosion of the range of the $-5/3$ energy spectra with downstream distance is clear. Moreover, we confirm that the selection of the filter window size will barely influence our above conclusions. In fact, owing to the low Reynolds number and the limited streamwise length, the variation of the range of the $-5/3$ power-law spectra cannot be expected to be too significant. It is unclear whether the spectra in the spanwise and cross stream velocity components reveal the same $-5/3$ scaling behavior as the streamwise components. This research direction is left for future work.

In a previous experimental study on grid-generated turbulence at a much higher Reynolds number [22], a similar but more significant observation is reported. That is, the energy spectrum exhibits a $-5/3$ power-law slope over one decade at the location where the turbulence is highly inhomogeneous. Moreover, with increasing downstream distance, grid-generated turbulence becomes Gaussian distributed. The corresponding range of the $-5/3$ power law (or $2/3$ power law in physical space), however, appears to be eroded. We want to mention that in previous studies on the spatial origin of the $-5/3$ spectra, wake-related flows (grid-generated turbulence [18,22,26,28] and flow behind a square prism [55]) are extensively studied. Here, we further show that a similar finding can be found in an essentially different kind of flow (i.e., dual-plane jet flow), somehow implying that the occurrence of the $-5/3$ spectra in a turbulent region where Kolmogorov's assertion does not hold appears to be universal.

To study what size motions are responsible for the nonzero Gaussian distribution, we employ an eight-order bidirectional filter with zero lag. The velocities passing low-pass and high-pass filters are denoted by $u'_>$ and $u'_<$, respectively. To study the evolution of the $-5/3$ scaling, the cutoff frequency is set to $f L_0/U_J = 0.3$. The spectra of the original signal u', low-pass signal $u'_>$, and high-pass signal $u'_<$ are plotted in Fig. 26, which indicates that the high-order filter selected can indeed efficiently remove the undesired components. The skewness and kurtosis of u', $u'_>$, and $u'_<$ are given in Table III. Take, for instance, the skewness of $u'_>$, $S(u'_>) = \langle u'^3_> \rangle / \langle u'^2 \rangle^{3/2}$. According to this definition, the skewness of u' can be written

$$S(u') = S(u'_>) + S(u'_<) + \frac{3\langle u'_> u'^2_< \rangle}{\langle u'^2 \rangle^{3/2}} + \frac{3\langle u'^2_> u'_< \rangle}{\langle u'^2 \rangle^{3/2}}. \tag{1}$$

The third term $S_{12} = 3\langle u'_> u'^2_< \rangle / \langle u'^2 \rangle^{3/2}$ and fourth term $S_{21} = 3\langle u'^2_> u'_< \rangle / \langle u'^2 \rangle^{3/2}$ on the right-hand side of Eq. (1) reflect the correlation between the large-scale and small-scale motions. Thus, $S(u')$

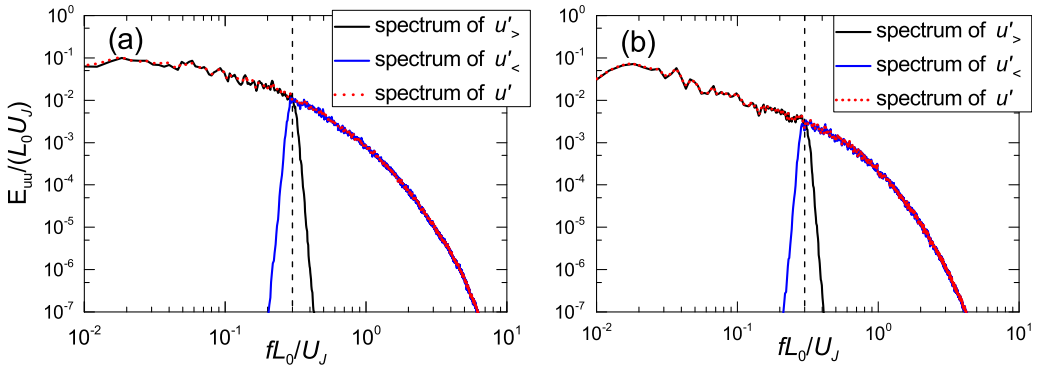

FIG. 26. Spectra of $u'_>$ and $u'_<$ at two streamwise locations, (a) $X/L_0 = 12$ and (b) $X/L_0 = 25$, for the case with $L_d/L_0 = 6$. For comparison, the corresponding unfiltered spectra (represented by the red dotted lines) are also plotted. The vertical dashed lines indicate the cutoff frequency $fL_0/U_J = 0.3$.

contains contributions from large-scale signal $u'_>$, small-scale signal $u'_<$, and their separate scale-scale correlations. For computation, the skewness of full signal u' can be decomposed as

$$S(u') = S(u'_>) + S(u'_<) + S_{12} + S_{21} + \mathcal{R}, \tag{2}$$

where $\mathcal{R}$ is the residual term, which would arise because of numerical errors associated with filtering operations. It might be worth mentioning that by now interactions between large and small scales are mainly investigated in turbulent boundary layers [56–58].

The positive value of the skewness $S(u')$ at $X/L_0 = 12$ is related to the large-scale motions, as can be seen from Table III. What is perhaps surprising is that at $X/L_0 = 25$, $S(u'_>)$ acquires a non-negligible negative value, $S(u'_>) = -0.10$, albeit $S(u') \simeq 0$. Downstream of the location $X/L_0 = 25$, for the case with $L_d/L_0 = 6$, the skewness of u' will become negative, as suggested by Fig. 10. The behavior of large-scale motions at $X/L_0 = 25$ may reflect this evolution tendency. Another interesting finding is that at $X/L_0 = 12$ and 25, the probability distributions of the small-scale motions are symmetrical since $S(u'_<)$ is negligibly small when compared with $S(u'_>)$.

It can be seen from Fig. 25(b) that the deterioration of the $-5/3$ power law occurs at large scales. According to the energy cascade of Kolmogorov and Richardson [49,59], on average energy is continually transferred from large scales to small scales. Thus, we may conclude a possible connection of the nonzero values of skewness to changes in the spectra shape at large scales. However, still we cannot exclude other possibilities; for example, these changes, in larger scales, may also be due to the downstream changes in the mean flow affecting how energy transferred to smaller scales.

To investigate the small-scale intermittency, we then examine the increments of the streamwise velocity fluctuations $\Delta u'(X, r)$, with $\Delta u'(X, r) = u'(X + r) - u'(X)$. Hence, $\Delta u'$ is a function of both the streamwise location X and longitudinal separation r. The PDFs of the increments of the streamwise velocity fluctuations at $X/L_0 = 12$ and 25 along the centerline are plotted. By comparing Figs. 27(a) and 27(b), one can see that PDFs for all r at $X/L_0 = 12$ are much fatter than the corresponding PDFs at $X/L_0 = 25$. The broad skirts found at $X/L_0 = 12$ indicate that for

TABLE III. Terms in Eq. (2) (i.e., $S(u')$, $S(u'_>)$, $S(u'_<)$, S_{12}, S_{21}, and $\mathcal{R}$) at $X/L_0 = 12$ and 25.

Location	$S(u')$	$S(u'_>)$	$S(u'_<)$	S_{12}	S_{21}	$\mathcal{R}$
$X/L_0 = 12$	0.46	0.25	0.0041	0.068	0.033	0.10
$X/L_0 = 25$	0.051	−0.10	0.0031	0.032	0.033	0.08

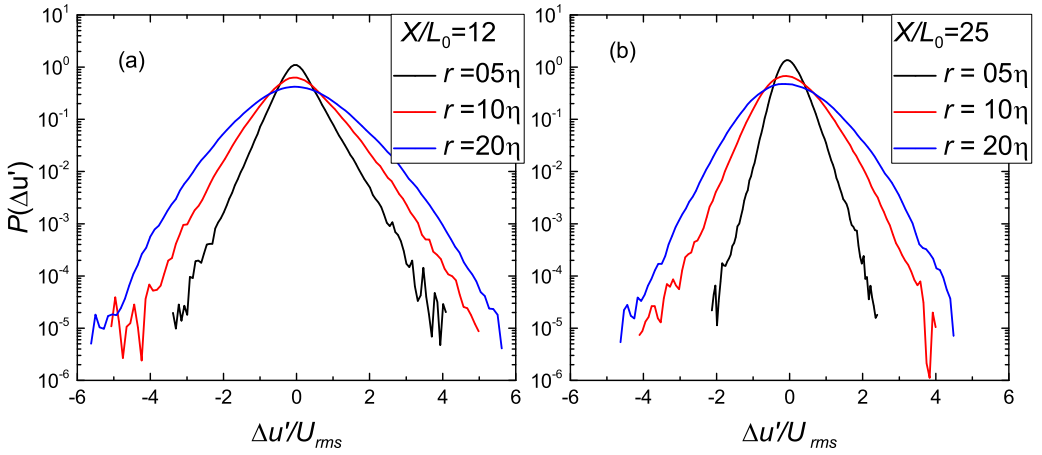

FIG. 27. PDFs of the increments of the velocity fluctuations at $X/L_0 = 12$ and 25 for the case with $L_d/L_0 = 6$. The separation distance r is using the Kolmogorov scale η with respect to the downstream coordinate, that is, $\eta = \eta(X/L_0)$.

all three scales investigated, the spatial intermittency is more pronounced. Previous studies [60–62] suggested that the small-scale intermittency is closely associated with the anomaly of scaling exponents of high-order structure functions (e.g., 4/5 law for the third-order structure function). We show that the small-scale intermittency seems not to affect the appearance of the $-5/3$ power law.

V. CONCLUSION

The streamwise evolutions of the statistical characteristics of dual-plane jet flows with different separation lengths (i.e., $L_d/L_0 = 4$, 6, and 8) are investigated by means of DNS. The jet-interaction scale X_* is introduced, and we are the first to show that in the case of plane jet interaction the variation of various statistics along the centerline can be collapsed when the downstream distance is normalized by X_*. This observation could directly explain the linear relationship between the downstream distance of the merge point X_{mp} and the separation length L_d.

To reveal the evolution mechanism of the velocity fluctuations in a dual-plane jet flow, the case with $L_d/L_0 = 6$ is extensively studied and its centerline characteristics are investigated in great detail. Close to the inlet at $X/L_0 = 7$, the flow along the centerline is intermittent ($\gamma \simeq 0.1$) and the corresponding negatively skewed probability distributions are generated by the alternation of the recirculation vortices' locations. At $X/L_0 = 12$, where the turbulence intensity and the mean pressure reach their maximum values, owing to stable junction of the two jets, the flow field is always turbulent ($\gamma \simeq 1$) and positively skewed probability distribution is identified. The positively skewed probability distribution could emerge when the faster neighboring fluid particles travel toward the centerline, accompanied by the appearance of a "heart" shape of the joint PDFs of u' and v'.

The above-mentioned formation mechanisms are not trivial, considering the observation that the skewness of the velocity fluctuation is closely related to the spatial origin of the $-5/3$ energy spectra [22,26–28]. In this study, for the case with $L_d/L_0 = 6$, the energy spectrum at $X/L_0 = 12$ acquires the $-5/3$ power law with a range for approximate half a decade, even though the flow is inhomogeneous and still spatially developing along with the fact that the local Reynolds number is only around 45. The term "developing" is used rather loosely to indicate that the turbulent flow is still in a state of transition at $X/L_0 = 12$, since at a sufficiently far downstream location, the dual-plane jet flow would eventually develop into a single-plane jet flow. Changes in spectral behavior appear to coincide with changes in high-order statistics, namely, $S(u')$ of the velocity. It is hard to

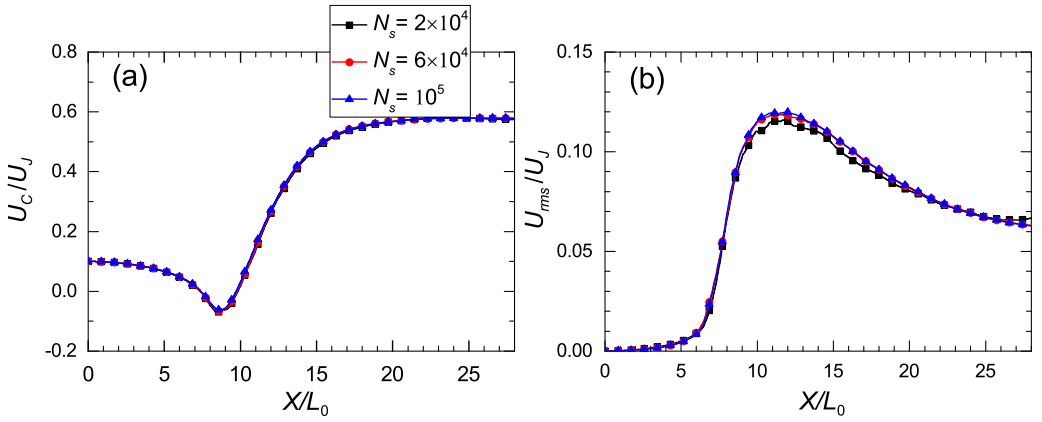

FIG. 28. Streamwise evolution of the centerline statistics (a) U_C/U_J and (b) U_{rms}/U_J corresponding to different time steps N_s and averaged over Z for the case with $L_d/L_0 = 6$.

imagine the interaction pattern revealed here (i.e., heart shape of the joint PDFs of u' and v') being unimportant in the formation of the $-5/3$ power-law spectra. This work therefore can be viewed as a complementary study of the existing investigations on the spatial origin of the $-5/3$ power-law spectra.

Scale-by-scale energy budget in the jet-interaction region (e.g., $X/L_0 \simeq 12$ for the case with $L_d/L_0 = 6$), where the turbulent flow is still developing, is an important issue. This research direction (e.g., Karman-Howarth-Monin-Hill equation) should be pursued in future works.

ACKNOWLEDGMENTS

This work was in part supported by the National Natural Science Foundation of China (No. 11802133), the Natural Science Foundation of Jiangsu Province (No. BK20180454), and the Fundamental Research Funds for the Central Universities (No. 30918011325). The authors would like to acknowledge an anonymous referee for many important comments. In particular, the idea concerning scale decomposition that we explored in Sec. IV is truly insightful.

APPENDIX: STATISTICAL CONVERGENCE

In this work, the statistics are averaged over time (a total of 10^5 time steps) and Z direction. To assess the convergence of the numerical data, the centerline evolutions of the first-, second-, third-, and fourth-order one-point statistics (i.e., U, U_{rms}, S_u, and F_u) for the case with $L_d/L_0 = 6$, which are averaged over different time steps (i.e., $N_s = 2\times10^4$, 6×10^4, and 10^5) and also Z direction, are plotted in Figs. 28 and 29.

Figure 28(a) implies that within the streamwise extent considered the averaged result of U appears to acquire satisfactory statistical convergence for even 2×10^4 steps. As presented in Fig. 28(b), the profiles of U_{rms} corresponding to 6×10^4 and 10^5 steps collapse together, indicating a good level of convergence is obtained. Compared with the well-converged low-order statistics (i.e., U and U_{rms}), the profiles of S_u and F_u are not smooth and not converged enough, especially at locations close to the inlet. As can be seen from Figs. 29(a) and 29(b), reasonably good level of convergence at $N_s = 10^5$ is obtained in the region $X/L_0 \geqslant 7$ whereas in the upstream region (i.e., $X/L_0 < 7$) the values of S_u and F_u are still dependent on the selection of N_s. This dependence at $X/L_0 < 7$ may find its roots in the rare bursts of the large negative u', which can be numerically highly demanding. However, it must be pointed out that the lack of convergence for S_u and F_u at $X/L_0 < 7$ is unlikely to affect our main conclusions of this work since the two different time

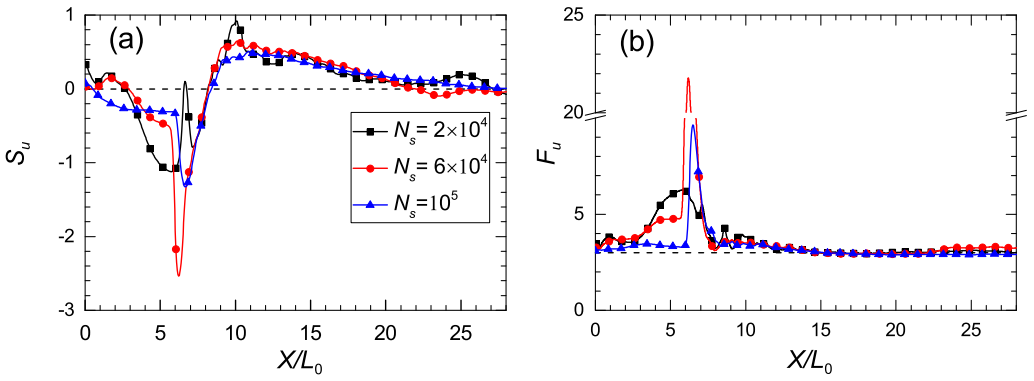

FIG. 29. Streamwise evolution of the centerline statistics (a) S_u and (b) F_u, corresponding to different time step N_s and averaged over Z for the case with $L_d/L_0 = 6$. The two dashes indicate, respectively, $S_u = 0$ and $F_u = 3$.

steps, $N_s = 6\times10^4$ and 10^5, return similar evolution tendency and the corresponding profiles are in quantitative agreement with each other.

[1] C. S. Wang, Y. F. Lin, and M. J. Sheu, Measurements of turbulent inclined plane dual jets, Exp. Fluids **16**, 27 (1993).

[2] D. Erdem and V. Ath, Interaction of two parallel rectangular jets, in Proceedings of 23rd International Congress of Aeronautical Sciences, Sep. 8–13, 2002, Toronto, Canada, 2002.

[3] T. Mondal, M. K. Das, and A. Guha, Periodic vortex shedding phenomenon for various separation distances between two plane turbulent parallel jets, Int. J. Heat Mass Transfer **99**, 576 (2016).

[4] D. R. Miller and E. W. Comings, Force-momentum fields in a dual-jet flow, J. Fluid Mech. **7**, 237 (1960).

[5] E. Tanaka, The interference of two dimensional parallel jets (1st report, Experiments on dual jet), Bull. JSME **13**, 272 (1970).

[6] E. Tanaka, The interference of two dimensional parallel jets (2nd report, Experiments on the combined flow of dual jet), Bull. JSME **17**, 920 (1974).

[7] N. E. Bunderson and B. L. Smith, Passive mixing control of plane parallel jets, Exp. Fluids **39**, 66 (2005).

[8] M. Soltys and J. Crimaldi, Joint probabilities and mixing of isolated scalars emitted from parallel jets, J. Fluid Mech. **769**, 130 (2015).

[9] N. B. Kaye and P. F. Linden, Coalescing axisymmetric turbulent plumes of vortex, J. Fluid Mech. **502**, 41 (2003).

[10] A. Karimpour, N. B. Kaye, and A. A. Khan, CFD study of merging turbulent plane jets, J. Hydraul. Eng. **137**, 381 (2010).

[11] Z. Baratian-Ghorghi, N. B. Kaye, A. A. Khan, and J. R. Smith, The merging of two unequal axisymmetric parallel turbulent jets, J. Hydro. Dyn. **24**, 257 (2012).

[12] G. Comte-Bellot and S. Corrsin, The use of a contraction to improve isotropy in grid-generated turbulence, J. Fluid Mech. **25**, 657 (1966).

[13] D. Hurst and J. C. Vassilicos, Scalings and decay of fractal-generated turbulence, Phys. Fluids **19**, 035103 (2007).

[14] N. Mazellier and J. C. Vassilicos, Turbulence without Richardson-Kolmogorov cascade, Phys. Fluids **22**, 075101 (2010).

[15] P. C. Valente and J. C. Vassilicos, The decay of turbulence generated by a class of multiscale grids, J. Fluid Mech. **687**, 300 (2011).

[16] K. Nagata, Y. Sakai, T. Inaba, H. Suzuki, O. Terashima, and H. Suzuki, Turbulence structure and turbulence kinetic energy transport in multiscale/fractal-generated turbulence, Phys. Fluids **25**, 065102 (2013).
[17] R. Gomes-Fernandes, B. Ganapathisubramani, and J. C. Vassilicos, Particle image velocimetry study of fractal-generated turbulence, J. Fluid Mech. **711**, 306 (2012).
[18] R. Gomes-Fernandes, B. Ganapathisubramani, and J. C. Vassilicos, Evolution of the velocity-gradient tensor in a spatially developing turbulent flow, J. Fluid Mech. **756**, 252 (2014).
[19] K. Nagata, T. Saiki, Y. Sakai, Y. Ito, and K. Iwano, Effects of grid geometry on non-equilibrium dissipation in grid turbulence, Phys. Fluids **29**, 015102 (2017).
[20] S. Laizet, J. C. Vassilicos, and C. Cambon, Interscale energy transfer in decaying turbulence and vorticity-strain-rate dynamics in grid-generated turbulence, Fluid Dyn. Res. **45**, 061408 (2013).
[21] S. Laizet, J. Nedić, and J. C. Vassilicos, Influence of the spatial resolution on fine-scale features in DNS of turbulence generated by a single square grid, Int. J. Comput. Fluid Dyn. **29**, 286 (2015).
[22] S. Laizet, J. Nedić, and J. C. Vassilicos, The spatial origin of $-5/3$ spectra in grid-generated turbulence, Phys. Fluids **27**, 065115 (2015).
[23] Y. Zhou, K. Nagata, Y. Sakai, H. Suzuki, Y. Ito, O. Terashima, and T. Hayase, Development of turbulence behind the single square grid, Phys. Fluids **26**, 045102 (2014).
[24] Y. Zhou, K. Nagata, Y. Sakai, H. Suzuki, Y. Ito, O. Terashima, and T. Hayase, Relevance of turbulence behind the single square grid to turbulence generated by regular and multiscale grids, Phys. Fluids **26**, 075105 (2014).
[25] Y. Zhou, K. Nagata, Y. Sakai, Y. Ito, and T. Hayase, On the evolution of the invariants of the velocity gradient tensor in single-square-grid-generated turbulence, Phys. Fluids **27**, 075107 (2015).
[26] Y. Zhou, K. Nagata, Y. Sakai, Y. Ito, and T. Hayase, Spatial evolution of the helical behavior and the $2/3$ power law in single-square-grid-generated turbulence, Fluid Dyn. Res. **48**, 021404 (2016).
[27] Y. Zhou, K. Nagata, Y. Sakai, Y. Ito, and T. Hayase, Enstrophy production and dissipation in developing grid-generated turbulence, Phys. Fluids **28**, 025113 (2016).
[28] I. Paul, G. Papadakis, and J. C. Vassilicos, Genesis and evolution of velocity gradients in near-field spatially developing turbulence, J. Fluid Mech. **815**, 295 (2017).
[29] T. Watanabe, Y. Sakai, K. Nagata, Y. Ito, and T. Hayase, Enstrophy and passive scalar transport near the turbulent/non-turbulent interface in a turbulent planar jet flow, Phys. Fluids **26**, 105103 (2014).
[30] T. Watanabe, Y. Sakai, K. Nagata, Y. Ito, and T. Hayase, Reactive scalar field near the turbulent/non-turbulent interface in a planar jet with a second-order chemical reaction, Phys. Fluids **26**, 105111 (2014).
[31] T. Watanabe, Y. Sakai, K. Nagata, H. Suzuki, Y. Ito, O. Terashima, and T. Hayase, Vortex stretching and compression near the turbulent/non-turbulent interface in a planar jet, J. Fluid Mech. **758**, 754 (2014).
[32] S. Stanley, S. Sarkar, and J. P. Mellado, A study of the flow field evolution and mixing in a planar turbulent jet using direct numerical simulation, J. Fluid Mech. **450**, 377 (2002).
[33] B. da Silva and O. Métais, On the influence of coherent structures upon interscale interactions in turbulent plane jets, J. Fluid Mech. **473**, 103 (2002).
[34] P. Moin and K. Mahesh, Direct numerical simulation: A tool in turbulence research, Annu. Rev. Fluid Mech. **30**, 539 (1998).
[35] M. Klein, A. Sadiki, and J. Janicka, A digital filter based generation of inflow data for spatially developing direct numerical or large eddy simulations, J. Comput. Phys. **186**, 652 (2003).
[36] A. Kempf, M. Klein, and J. Janicka, Efficient generation of initial and inflow conditions for transient turbulent flows in arbitrary geometries, Flow, Turbul. Combust. **74**, 67 (2005).
[37] R. R. Taveira and C. B. da Silva, Kinetic energy budgets near the turbulent/nonturbulent interface in jets, Phys. Fluids **25**, 015114 (2013).
[38] T. Kajishima and K. Taira, *Computational Fluid Dynamics: Incompressible Turbulent Flows* (Springer, Switzerland, 2017).
[39] T. Yoshida, T. Watanabe, and I. Nakamura, Numerical study of outflow boundary conditions for time dependent incompressible flows, Trans. Japan Soc. Mech. Eng. B **61**, 2887 (1995).
[40] S. Laizet and E. Lamballais, High-order compact schemes for incompressible flows: A simple and efficient method with the quasi-spectral accuracy, J. Comput. Phys. **228**, 5989 (2009).

[41] S. Laizet, E. Lamballais, and J. C. Vassilicos, A numerical strategy to combine high-order schemes, complex geometry, and parallel computing for high resolution DNS of fractal generated turbulence, Comput. Fluids **39**, 471 (2010).
[42] S. Laizet and N. Li, INCOMPACT3D, a powerful tool to tackle turbulence problems with up to $O(10^5)$ computational cores, Int. J. Numer. Methods Fluids **67**, 1735 (2011).
[43] S. K. Lele, Compact finite difference schemes with spectral-like resolution, J. Comput. Phys. **103**, 16 (1992).
[44] J. Kim and P. Moin, Application of a fractional-step method to incompressible Navier-Stokes equations, J. Comput. Phys. **59**, 308 (1985).
[45] E. Lamballais, V. Fortuné, and S. Laizet, Straightforward high-order numerical dissipation via the viscous term for direct and large eddy simulation, J. Comput. Phys. **230**, 3270 (2011).
[46] E. Gutmark and I. Wygnansky, The planar turbulent jet, J. Fluid Mech. **73**, 465 (1976).
[47] R. Ramparian and M. S. Chandrasekhara, LDA measurements in plane turbulent jets, ASME J. Fluids Eng. **107**, 264 (1985).
[48] C. B. da Silva and J. C. F. Pereira, Invariants of the velocity-gradient, rate-of-strain, and rate-of-rotation tensors across the turbulent/nonturbulent interface in jets, Phys. Fluids **20**, 055101 (2008).
[49] H. Tennekes and J. L. Lumley, *A First Course in Turbulence* (MIT Press, Cambridge, MA, 1972).
[50] M. Bisoi, M. K. Das, S. Roy, and D. K. Patel, Turbulent statistics in flow field due to interaction of two plane parallel jets, Phys. Fluids **29**, 125108 (2017).
[51] Y. F. Lin and M. J. Sheu, Interaction of parallel turbulent plane jets, AIAA J. **29**, 1372 (1991).
[52] G. Marsters, Interaction of two plane, parallel jets, AIAA J. **15**, 1756 (1977).
[53] Y. Zhou and J. C. Vassilicos, Related self-similar statistics of the turbulent/non-turbulent interface and the turbulence dissipation, J. Fluid Mech. **821**, 440 (2017).
[54] R. R. Taveira, J. S. Diogo, D. C. Lopes, and C. B. da Silva, Lagrangian statistics across the turbulent-nonturbulent interface in a turbulent plane jet, Phys. Rev. E **88**, 043001 (2013).
[55] F. A. Portela, G. Papadakis, and J. C. Vassilicos, The turbulence cascade in the near wake of a square prism, J. Fluid Mech. **825**, 315 (2017).
[56] S. Duvvuri and B. J. McKeon, Triadic scale interactions in a turbulent boundary layer, J. Fluid Mech. **767**, R4 (2015).
[57] R. Mathis, N. Hutchins, and I. Marusic, Large-scale amplitude modulation of the small-scale structures in turbulent boundary layers, J. Fluid Mech. **628**, 311 (2009).
[58] P. Schlatter and R. Örlü, Quantifying the interaction between large and small scales in wall-bounded turbulent flows: A note of caution, Phys. Fluids **22**, 051704 (2010).
[59] U. Frisch, *Turbulence: The Legacy of A. N. Kolmogorov* (Cambridge University Press, Cambridge, UK, 1995).
[60] K. R. Sreenivasan and R. A. Antonia, The phenomenology of small-scale turbulence, Annu. Rev. Fluid Mech. **29**, 435 (1997).
[61] K. R. Sreenivasan, Fluid turbulence, Rev. Mod. Phys. **71**, S383 (1999).
[62] M. Kholmyansky and A. Tsinober, On an alternative explanation of anomalous scaling and how well defined is the concept of inertial range, Phys. Lett. A **373**, 2364 (2009).